

Discrimination of neutron from gamma radiation in diamond detectors

Ivanković, Karla

Master's thesis / Diplomski rad

2022

Degree Grantor / Ustanova koja je dodijelila akademski / stručni stupanj: **University of Zagreb, Faculty of Science / Sveučilište u Zagrebu, Prirodoslovno-matematički fakultet**

Permanent link / Trajna poveznica: <https://um.nsk.hr/um:nbn:hr:217:536593>

Rights / Prava: [In copyright](#) / [Zaštićeno autorskim pravom.](#)

Download date / Datum preuzimanja: **2025-01-18**



Repository / Repozitorij:

[Repository of the Faculty of Science - University of Zagreb](#)



UNIVERSITY OF ZAGREB
FACULTY OF SCIENCE
DEPARTMENT OF PHYSICS

Karla Ivanković

Discrimination of neutron from gamma
radiation in diamond detectors

Master Thesis

Zagreb, 2022

SVEUČILIŠTE U ZAGREBU
PRIRODOSLOVNO-MATEMATIČKI FAKULTET
FIZIČKI ODSJEK

Karla Ivanković

Razlikovanje neutronske od gama zračenja u
dijamantnim detektorima

Diplomski rad

Zagreb, 2022

UNIVERSITY OF ZAGREB
FACULTY OF SCIENCE
DEPARTMENT OF PHYSICS

INTEGRATED UNDERGRADUATE AND GRADUATE UNIVERSITY
PROGRAMME IN PHYSICS

Karla Ivanković

Master Thesis

**Discrimination of neutron from
gamma radiation in diamond
detectors**

Advisor: Dr. sc. Georgios Provatas, Research Associate

Co-Advisor: Dr. sc. Petar Žugec, Assistant Professor

Master Thesis grade: _____

Committee: 1. _____

2. _____

3. _____

Master Thesis defence date: _____

Zagreb, 2022

Firstly, I would like to thank my mentor dr. sc. Georgios Provatas for his time and guidance as well as all the knowledge he generously shared. Also, I would like to thank everybody in the Laboratory for ion beam interactions at Ruđer Bošković Institute for all their help, especially dr. sc. Milko Jakšić and dr. sc. Andreo Crnjac. Finally, a big thank you to my mom, dad, sister and Marko for their love and support.

Razlikovanje neutronske od gama zračenja u dijamantnim detektorima

Sažetak

Cilj ovog rada je ispitivanje novih mogućih načina diskriminacije neutronske od gama zračenja u dijamantnim detektorima. Novi patentirani dijamantni detektor dizajniran je i ispitan pomoću protonskih snopova različitih energija ubrzanih korištenjem akceleratora Tandem Van de Graaf i Tandetron u eksperimentalnim komorama Laboratorija za interakcije ionskih snopova Instituta Ruđer Bošković u Zagrebu. Za potvrdu optimalnog dizajna geometrije napravljene su Monte-Carlo simulacije pomoću alata kao što su GRAS, Geant4 i ROOT za definiranje geometrije detektora, izvora i analizu, kao i SRIM programski paket.

Ključne riječi: neutronske zračenje, gama zračenje, protoni, dijamantni detektori, poluvodiči, IBIC, STIM, ionski snopovi, Monte-Carlo simulacije, akceleratori čestica, ionska mikroproba

Discrimination of neutron from gamma radiation in diamond detectors

Abstract

The purpose of this paper is to examine new possible ways of discrimination of neutron from gamma radiation in diamond detectors. A brand new patented diamond detector was designed and tested using proton beams of various energies accelerated using the Tandem Van de Graaf and Tandetron accelerators in experimental chambers of the Laboratory for ion beam interactions of the Rudjer Boskovic Institute in Zagreb. In order to corroborate that the geometry design was optimal for fast neutron and gamma ray discrimination, simulations were made using Monte-Carlo simulation tools GRAS, GEANT4 and CERN's scientific software framework ROOT as well as SRIM.

Keywords: neutron radiation, gamma radiation, protons, diamond detectors, semi-conductors, IBIC, STIM, ion beams, Monte-Carlo simulations, particle accelerators, ion microprobe

Contents

1	Introduction	1
2	Theoretical background	3
2.1	Ion interactions with matter	3
2.2	Interaction of neutrons with matter	5
2.3	Interaction of gamma rays with matter	5
2.4	Detectors and their properties	6
2.4.1	Semiconductor detectors	8
2.4.2	Surface barrier detectors (Silicon Surface Barrier - SSB)	10
2.4.3	Diamond detectors	10
2.4.4	Use of diamond detectors for detection of neutrons	11
3	Simulations and software	14
3.1	Reasoning behind simulations	14
3.2	Making of simulations and explanation	14
3.2.1	Geometry	14
3.2.2	Monte-Carlo Simulations	16
3.2.3	Results	17
3.3	SRIM Software Simulations	19
4	Experimental setup and method	23
4.1	Diamond detector configuration	23
4.1.1	Characteristics of the detector	23
4.1.2	Construction of the detector	24
4.2	Experiment at the Laboratory for ion beam interactions	25
4.2.1	Particle accelerators	25
4.2.2	Ion microprobe	28
4.2.3	Ion Beam Induced Charge Microscopy (IBIC)	31
4.2.4	Scanning Transmission Ion Microscopy (STIM)	31
4.2.5	Data acquisition and the electronic chain	31
4.2.6	Experimental setup and procedures	33
4.3	Experiments in coincidence mode	34

5 Results and discussion	36
6 Summary and outlook	45
6.1 Summary	45
6.2 Outlook	45
Appendices	46
A Detector geometry .c file	46
B Source .g4mac file	59
7 Prošireni sažetak	61
7.1 Uvod	61
7.2 Teorijska pozadina	62
7.2.1 Interakcije čestica i materije	62
7.2.2 Poluvodički i dijamantni detektori	63
7.3 Simulacije	65
7.4 Eksperimentalne metode i postav	66
7.5 Rezultati	68
7.6 Zaključak	70
Bibliography	72

1 Introduction

Semiconductor detectors are radiation detectors based on semiconductor materials (usually silicon or germanium and also diamond) and their properties. Their development began in the 1950s and continued rapidly with the commercial use beginning in the 1970s. They are used for the detection of charged particles since a charged particle traversing through the semiconductor material causes electromagnetic processes which can be observed and measured. Semiconductor detectors could also be used to detect uncharged particles such as neutrons and gamma rays but not directly as protons, electrons and other ions, but through detection of secondary charged particles that are formed due to elastic and inelastic scattering and other physical processes of neutrons and gamma rays in detector material. Diamond detectors are semiconductor detectors with great properties for neutron and gamma ray detection (and other ionizing radiation detection) due to their low leakage current and capacitance, high sensitivity, high radiation resistance as well as high temperature resistance. They can provide discrimination between different types of radiation as their pulse shape varies for different particles. This leads to an important use of diamond detectors in rough environments with a lot of incoming radiation, high temperatures and complicated backgrounds (e.g. fission and fusion reactors). This is exactly the motivation behind the detector configuration used in this paper, to investigate the possibility of detection of high energy neutrons in the presence of gamma radiation background. Currently, the conventional techniques applied for neutron-gamma discrimination are based on either the pulse shape discrimination techniques or through the measurement of secondary products with the addition of conversion layers such as ${}^6\text{LiF}$ and ${}^{10}\text{B}$. However their application is limited in the presence of radiation or temperature hard conditions. A diamond detector created to operate in the temperature range between 0 and 750K with a low efficiency for gamma radiation could be used in such complicated conditions. The main idea is to create such detector geometry for the discrimination of alpha particles (secondary particles created in neutron interaction with matter) from Compton electrons (secondary particles created in gamma ray interaction with matter). In the present work such prototype detector was constructed, based on the patent designed by dr. sc. Milko Jaksic, dr. sc. Georgios Provatas and dr. sc. Andreo Crnjac seen in Figure 1.1. In such a detector

neutrons will induce a signal in one of the electrodes while gamma rays will induce a signal in both electrodes. Moreover, the developed detector was characterized and tested by means of the IBIC technique microprobe setups in the Laboratory for ion beam interactions at the Rudjer Boskovic Institute Zagreb.

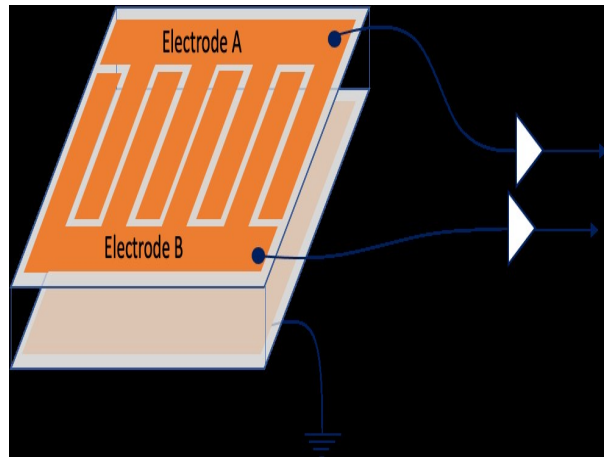


Figure 1.1: Proposed design of CVD diamond detector for discrimination of fast neutrons from gamma radiation by dr. sc. Milko Jaksic, dr. sc. Georgios Provatas and dr. sc. Andreo Crnjac.

2 Theoretical background

2.1 Ion interactions with matter

When charged particles pass through matter there are two main processes which result either in loss of energy by the particle or deflection of the particle from the incident direction through elastic scattering. These are results of inelastic collisions with free and atomic electrons and target atoms as well as elastic scattering. Other reactions which happen more rarely are Cherenkov radiation which occurs when the particle velocity in the material is greater than the speed of light in that material, nuclear reactions and bremsstrahlung ("deceleration radiation") which is the electromagnetic radiation caused by deceleration of charged particles when deflected by another charged particle.

For the operation of particle detectors it is important to understand ion interactions with matter and the effects of these processes, as well as processes caused by neutrons and gamma rays. Firstly some important definitions must be introduced starting with the cross section. The interaction cross section for a process essentially gives the measure of probability for a reaction to occur. The integral of the differential cross section gives the total cross section [25, p. 73]:

$$\sigma = \int \frac{d\sigma}{d\Omega} d\Omega \quad (2.1)$$

The energy loss of a charged particle transversing through a medium is described by the stopping power dE/dx , which can be electronic, nuclear or radiative. Electronic stopping power is caused by inelastic collisions between bound electrons in the medium and the ion moving through it. The projectile particle slows down due to ionization or excitation of target atoms. These collisions cause small energy loss per collision but a high number of collisions happen with small deviation of the projectile particle from the incident path. Nuclear stopping power involves the interaction between the projectile ion and the atoms or nucleus of the target elements, the stopping of the projectile particle is caused by inelastic scattering from the nuclei. The third type of stopping power, radiative, must be considered at very high ion energies and is due to bremsstrahlung in the electric field of the particles in the targeted material. Energy loss of protons in a material can be demonstrated using

SRIM, a software which will further explained in Section 3.3. The slowing down of protons in a solid material can be seen in Figure 2.1. Here the Bragg peak of pro-

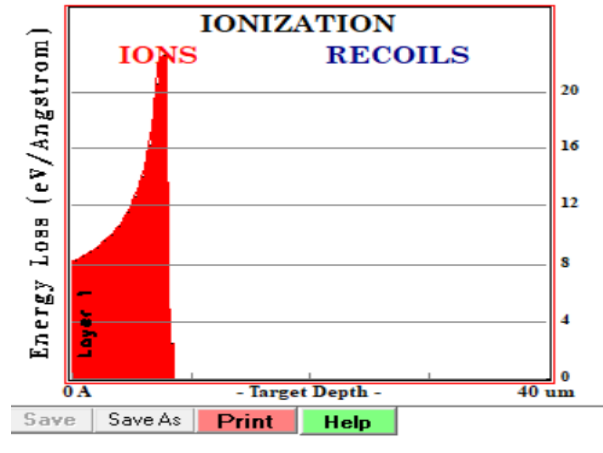


Figure 2.1: Proton energy loss in a solid material.

tons passing through matter can be defined as the prominent peak in Figure 2.1, and this peak occurs immediately before the ion completely stops. When it comes to ion stopping in solid materials at first, at high energies, electronic stopping dominates, the ion moves almost at a straight path, and as it slows down collisions with nuclei become possible and nuclear stopping starts, and eventually begins to dominate. The collisions of ions with atoms of the material cause the atoms to be moved from their positions in the lattice and this causes the production of further collisions cascades. Protons are positively charged particles which interact with matter predominantly in the following three ways: the inelastic Coulomb interaction with atomic electrons (Figure 2.2 (a)) which is the most dominant interaction, elastic Coulomb scattering with atomic nuclei (Figure 2.2 (b)) and non-elastic nuclear reactions (Figure 2.2 (c)). These three physical processes cause protons to lose energy and deflect while traversing matter.

When it comes to inelastic collisions with atomic electrons, protons (as well as other charged particles) lose energy following the Bethe-Bloch formula [25, p. 13]:

$$\frac{dE}{dx} \approx -4\pi\hbar^2c^2\alpha^2 \frac{nZ}{m_e v^2} \left[\ln \frac{2m_e c^2 \beta^2 \gamma^2}{I_e} - \beta^2 \right] \quad (2.2)$$

where $\frac{dE}{dx}$ is the mean energy loss per path length, v is the particle's velocity defined as βc , Z is the atomic number of the material, n is the number density, I_e is the average effective ionization potential of the material and α is the fine structure constant. The

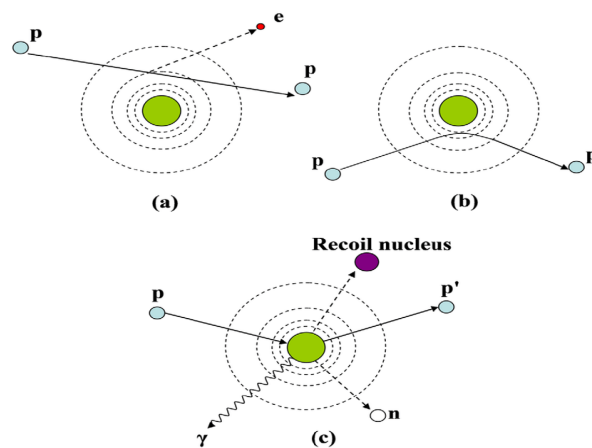


Figure 2.2: Proton interactions with matter illustrated: (a) inelastic Coulomb interaction, (b) elastic Coulomb scattering, (c) nuclear reactions.[10]

elastic scattering with atomic nuclei leads to the deflection of the charged particle from incident direction and depending on the thickness of absorbing material the scattering which occurs may be Coulomb or Rutherford. Lastly, nuclear reactions may happen with smallest probability out of these three processes and in that case the incident proton collides with the atomic nucleus creating new nuclides.

2.2 Interaction of neutrons with matter

Neutrons as electrically neutral particles do not interact with matter through Coulomb interactions but through the strong, short range force with nuclei. The main interactions with nuclei are elastic scattering, inelastic scattering, radiative neutron capture, nuclear reactions in which a neutron is captured and charged particles are emitted, fission and hadron shower production. Which of these processes happens depends greatly on neutron energy, for example for neutrons in the MeV region elastic scattering occurs, and for neutrons with energies above 100 MeV high energy hadron showers occur.

2.3 Interaction of gamma rays with matter

Gamma ray interactions are carried out with three processes; the photoelectric effect, Compton scattering and pair production. The photoelectric effect happens when an incident photon has the energy similar to the binding energy of an electron in the target atom, the gamma ray then ejects an electron from the atom. The energy of

the ejected atom is then $E=h\nu-E_B$ where ν is the frequency of the incident gamma radiation, h is the Planck's constant with the value $6.62607015 \cdot 10^{-34}m^2kg/s$ and E_B is the electron binding energy.

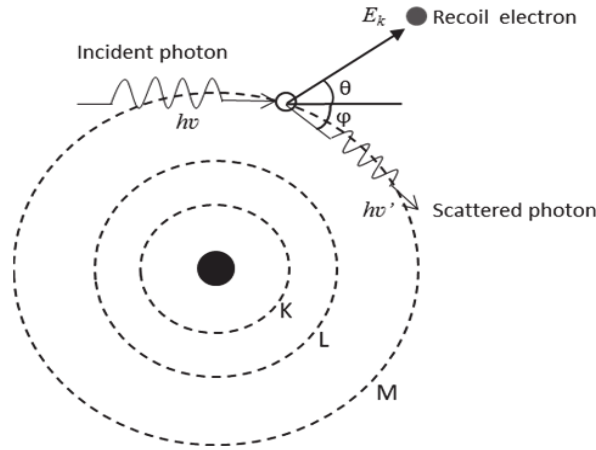


Figure 2.3: Illustration of Compton scattering.[5]

Pair production happens for highest energies of gamma rays ($> 1.022MeV$) [24] and the photon creates an electron-positron pair.

2.4 Detectors and their properties

The general principle on which ionizing radiation is detected is based on the conversion of the particle's energy to charge carriers within the detector's sensitive volume. This charge is collected by applying an electric field and then converted to a pulse using appropriate preamplifiers and amplifiers unit. This setup can be seen in Figure 2.4. The general properties of detectors which will be briefly discussed in the following subsection include sensitivity, energy resolution, Fano-factor, response function and time, efficiency and dead time. First important property of detectors is the capability of producing a usable signal for a given type of radiation and energy. Detectors are designed to be sensitive to certain types of radiation (proton, neutron, gamma etc.) in a particular energy range. In this range the detector should be able to produce a valid signal with high signal to noise ratio. The sensitivity of the detector depends on the cross section for ionizing reactions in the detector, on the detector material, inherent noise and protective material around the sensitive detecting area. The detector response is the relation between radiation energy and total charge (pulse height) of the output signal. Ideally any detector should have a

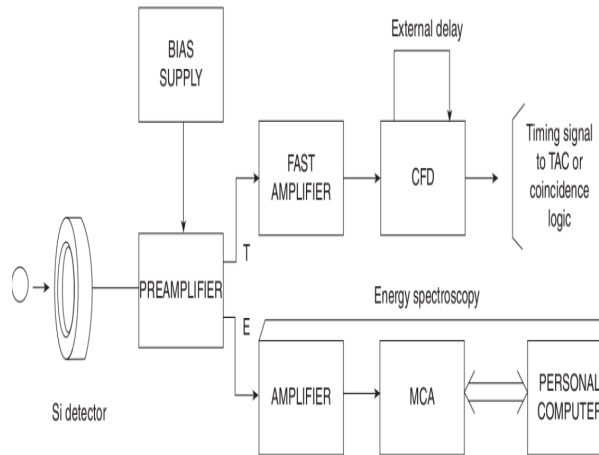


Figure 2.4: Circuitry for measurements with detectors for NIM electronics.

linear response which is the case in semiconductor detectors. Energy resolution is a measure of the ability of the detector to accurately determine the energy deposited in its sensitive volume. It is defined using Full Width Half Maximum of the energy peak (FWHM) and the maximum height of said peak (E).

$$Resolution = \frac{FWHM}{E} \tag{2.3}$$

How FWHM and maximum energy (E) are defined can be seen in Figure 2.5. With

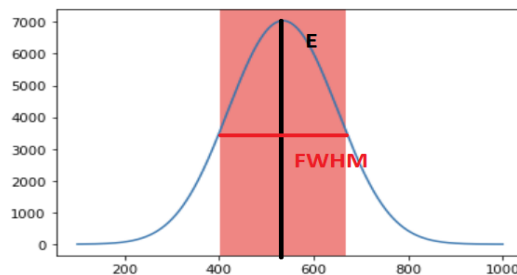


Figure 2.5: Defining full width half maximum (FWHM) and maximum energy peak (E).

the term detector efficiency one can consider the total or intrinsic efficiency. If one considers total efficiency it is the number of events registered by the detector divided by all events emitted by the ion source. This type of efficiency depends greatly on detector geometry. Intrinsic efficiency, on the other hand is the ratio of events registered by the detector and the number of events that reach the detector. Further, dead time corresponds to the time required by the detector, electronic chain and DAQ for

processing an event. The dead time depends on the detector's response time, being the time needed by the detector to form a signal, the settings of the DAQ, i.e. use of charge or current sensitive amplifiers, shaping time settings etc, as well as the count rate of a measurement. Determining dead time is important in order to know if the detector remains sensitive to other events during the duration of the pulse signal and typically is obtained by introducing the signal of a pulse generator in the detection electronic chain with a well known frequency. If the detector does not remain sensitive events are lost. Lastly, response time and function should be discussed. The response function is the spectrum of pulse heights the detector observes while being exposed to a radiation source. The response function depends on ion interactions with the detector material as well as the detector geometry.

2.4.1 Semiconductor detectors

Semiconductors are materials whose structure of the energy band is significantly different from that of the conductor and insulator. Insulators have a wide energy gap that prevents the transition of electrons from the valence to the conductive band. Conductors have an overlap between the two bands which allows transitions of electrons from the valence band to the conducting band. As is in the case with insulators, semiconductors have an energy gap, but it is much smaller and under the right conditions electrons can be excited and pass into the conductive band. Comparison of energy band structures for conductors, semiconductors and insulators can be seen in Figure 2.6. Important and useful property of semiconductor detectors is that a small

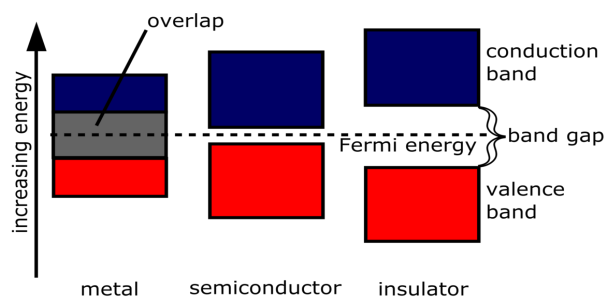


Figure 2.6: Energy band of insulators, conductors and semiconductors [11].

amount of energy is needed to create one electron-hole pair. This energy is called the w-value, and for silicon for example it is 3.62 eV [3] at a temperature of 300K and for diamond it is 13 eV [2]. Semiconductor detectors typically have a linear response

with respect to energy. If the voltage at the electrodes of the detector is V , n is the collection efficiency and the charge at the electrodes is $\frac{nE}{w}$ and C is the capacity of the depletion region then the following applies [3, p. 221]:

$$V = \frac{nE}{wC} \quad (2.4)$$

In semiconductor detectors it is also important to define the depletion region, as seen in Figure 2.7. A pn junction must be created using special techniques to ensure close contact between n-type and p-type semiconductors [3, p 215]. In such a junction the difference in electron and hole concentration between the n and p type semiconductors causes a diffusion of electrons towards the p-region and holes towards the n-doped region. After some time, this diffusion accumulates a negative charge on the p part of the junction and a positive charge on the n part of the junction. This accumulated charge at the edges of the junction creates an electric field that prevents further diffusion and leads to a stable charge distribution, and the area where the imbalance is established is called the depletion region. It acts as a radiation detector. When measuring on detectors, while they are at a potential, a weak, fluctuating

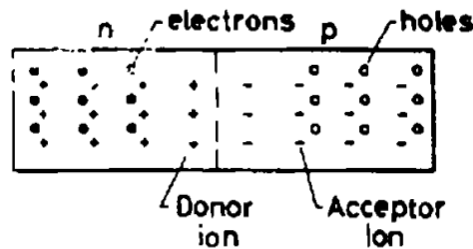


Figure 2.7: Depletion region.[3]

current flows through the semiconductor junctions, and that current is called leakage current and it acts as noise. The biggest cause of leakage currents are surface channels. Leakage current can also be caused by the movement of minority charge carriers, holes from the n-region to the p-region or electrons from the p-region to the n-region. It can also be a result of recombination of electron-hole pairs entering the depletion zone. The sensitivity of semiconductor detectors is almost 100%, they give excellent energy resolution, and what reduces it can be the noise of the electronics used or the leakage current.

2.4.2 Surface barrier detectors (Silicon Surface Barrier - SSB)

Surface barrier detectors are the most commonly used type of semiconductor (silicon) particle detectors in accelerator laboratories and ion beam applications. They operate based on a junction between a semiconductor and metal (e.g. n-doped silicon and gold or p.doped silicon with aluminum) which have different Fermi levels causing a contact electromagnetic field between the two layers similar to the one in the np junction with the depletion region created extending completely into the semiconductor. These junctions are called Schottky barriers and have similar properties to np junctions [3]. SSB detectors can be operated in three modes based on the voltage applied, partially depleted, fully depleted and over depleted. In Figure 2.8 a

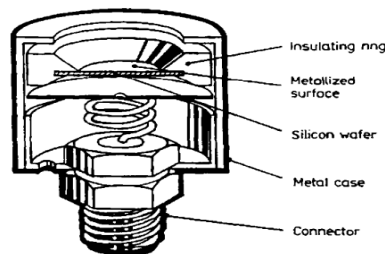


Figure 2.8: Surface barrier detector.[3]

surface barrier detector can be seen, it consists of a insulator ring, metalized surface, a silicon wafer, a metal case and a connector.

2.4.3 Diamond detectors

Diamond detectors are semiconductor detectors with electron-hole production energy 13 eV/pair^1 . Their operation principle is shown in Figure 2.9: the incident particle ionizes electrons and holes which drift towards the electrodes due to the electric field created from the applied bias voltage and when connected to a charge sensitive amplifier, they induce a voltage signal, proportional to the collected charge. Currently, diamond detectors produced by means of chemical vapor deposition (CVD) technique enable the fabrication of thin diamond films of a few μm up to $500 \mu\text{m}$ thickness. As such it is important to note that a high energy incident particle will ionize the diamond with only a part of its energy, and if the incident particle has

¹[2]

lower energy it will deposit all its energy in the detector. Diamond detectors have an intrinsic detection efficiency of 100% when it comes to detection of charged particles. The band gap of diamonds is 5.5 eV which is greater than silicon (which has the band

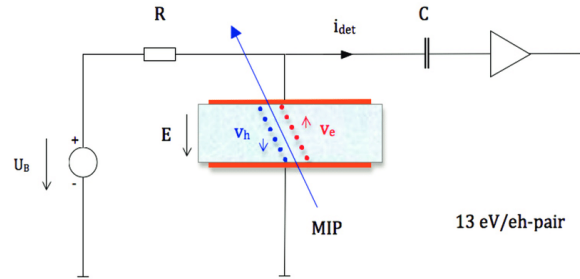


Figure 2.9: Principle of operation of diamond detectors [4].

gap 1.12 eV) resulting in higher signal to noise ratios compared to Si detectors, hole mobility is $2100 \text{ cm}^2 \text{Vs}^{-1}$ and electron mobility is somewhat greater, $2400 \text{ cm}^2 \text{Vs}^{-1}$. The breakdown field is 10^7 V/mm which makes high electric fields possible. Intrinsic carrier density of diamond is less than 10^3 cm^{-3} which means lower noise during operation. The resistivity is higher than $10^{12} \Omega$ and the dielectric constant is 5.7 which means diamond detectors have a lower capacitance than silicon detectors with the dielectric constant of 11.9. The displacement energy of 43 eV/atom leads to less damage to the crystal as opposed to silicon (13-20 eV/atom). is significantly greater compared to silicon. As such, diamond detectors are radiation harder than silicon and are perfect candidates for applications in high radiation environments. As mentioned before, the energy for pair production in diamond is 13 eV/pair which is the only down side compared to silicon properties (3.6 eV/pair) as it means lower signal amplitude. The diamond is also physically harder as it was tested from 100 K to 1000 K [27, 28]. The aforementioned properties are summarized in Table 2.1.

2.4.4 Use of diamond detectors for detection of neutrons

As it was explained in Section 2.4.3 diamond is a very good material for particle detection due to its properties (low leakage current, band gap, carrier density, thermal conductivity, high radiation resistance, capacitance, electron-hole mobility, etc.). Neutron, and gamma rays as well, are not electrically charged and do not ionize the detector directly but rather cause the production of secondary charged particles (electrons, protons, alpha particles) once they are absorbed or scattered on the dia-

Property	Silicon	Diamond
Band gap (eV)	1.12	5.5
Breakdown field (V/mm)	$3 \cdot 10^5$	10^7
Intrinsic carrier density (cm^{-3})	$1.5 \cdot 10^{10}$	$< 10^3$
Mass density (g/cm^3)	2.33	3.52
Dielectric constant	11.9	5.7
Displacement energy (eV/atom)	13-20	43
Energy to create e-h pair (eV)	3.6	13
Resistivity (Ω)	$2.23 \cdot 10^5$	$> 10^{12}$
Hole mobility (em^2Vs^{-1})	480	2100
Electron mobility (em^2Vs^{-1})	13350	2400

Table 2.1: Comparison of properties of diamond and silicon.[1]

mond. Neutrons are then detected through the detection of these secondary charged particles. Fast neutrons which are neutrons with the kinetic energy above 1 keV are generally detected due to inelastic and elastic scattering on the diamond. Inelastic reactions with carbon and neutrons :



are the cause of alpha particle production in diamond detectors. Once alpha particles are detected this indicates the presence of neutrons. Other reactions with carbon and neutrons can also produce secondary charged particles (electrons and protons) which can then be detected. Those reactions are:



These reactions can be seen in Figure 2.10 which shows an experimental spectrum of 14.1 MeV neutrons collected at RBI's neutron generator. The blue line shows the full spectrum and the orange corresponds to the one collected in coincidence with the associated alpha particle, i.e. the discriminated from gamma rays neutron spectrum.

These reactions cause the production of secondary charged particles (alpha particles)

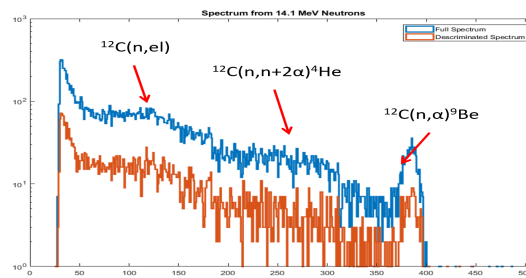


Figure 2.10: Measured energy spectrum for 14.1 MeV neutrons [6].

which are then used to detect neutrons. Gamma rays are on the other hand detected due to secondary particles they create while interacting with matter - Compton electrons. In a diamond detector with geometry shown in Figure 1.1 the alpha particles created in these reactions would induce a signal in one of the electrodes indicating the presence of neutrons, and electrons would induce a signal in both electrodes indicating gamma rays.

3 Simulations and software

3.1 Reasoning behind simulations

In order to determine the optimum configuration of the two top electrodes and estimate the discrimination performance of the developed detector, Monte Carlo simulations were carried out. The simulation setup was evaluated by comparing the simulation results with spectra obtained previously using Laboratory for ion beam interactions developed diamond detectors using the Rudjer Boskovic Institute neutron source.

3.2 Making of simulations and explanation

The simulations were carried out by means of Monte Carlo simulations using the ESA's Geant4-based tool GRAS². The geometry was prepared with CERN's scientific software framework ROOT³. The latter was also used for the analysis of the simulation results. In the following paragraphs, the steps that were followed for this study are described in detail.

3.2.1 Geometry

The geometry of the detector was made using the ROOT geometry manager. This package is used to build, browse, navigate and visualize various detector geometries and the corresponding materials. Before creating the detector geometry it is important to define "the world", so the first thing to do is loading the geometry library by using the following command:

```
gSystem->Load("libGeom");
```

After defining the world which is the volume surrounding the detector, the material of which the world is made of is defined as well as the state of the material in the following way:

```
TGeoMaterial *matVacuum = new
```

```
TGeoMaterial("Vacuum",1.01,1,1.e-25,TGeoMaterial::kMatStateGas,2.73,3.0e-18);
```

The materials made of single elements are constructed using TGeoMaterial and are

²<https://essr.esa.int/project/gras-geant4-radiation-analysis-for-space>

³<https://root.cern/>

defined by their atomic mass (A), charge (Z) and density (ρ).

The material of the world is vacuum and it is in the gaseous state. Volumes, basic components used in ROOT are implemented by the class TGeoVolume. The volumes have appointed shapes such as TGeoBBox (square shape), TGeoSphere (spherical shape), TGeoTrd1 (trapezoid shape) etc. The volumes defined in this case are 60 box shapes representing 60 stripes of the detector, 30 on one electrode, and 30 on the other. The box shape is built using TGeoBBox class with three parameters, dx, dy, dz which represent half-lengths on x, y and z axis, or in this case the parameters are named length, width and thick (length, width and thickness of each strip):

```
TGeoBBox *det1 = new TGeoBBox("det1", length, width, thick);
```

Each strip of the detector is made of diamond, which is defined in two steps. First step is defining carbon using a pre-built table of elements provided by TGeoManager class:

```
TGeoElementTable *table = new TGeoElementTable(200);
```

```
TGeoElement *carbon = table->FindElement("C");
```

and the second step is defining diamond material as carbon with the density corresponding to diamond density (3.5 g/cm³) in solid state as follows:

```
TGeoMaterial *matDiamond = new TGeoMaterial("Carb", carbon, 3.5);
```

```
matDiamond->SetState(TGeoMaterial::kMatStateSolid);
```

After creating the geometry of the detector and the world around it it's possible to visualize it using ROOT's OGL viewer, and it can be extracted to a Geometry Description Markup Language (GDML) format to be later imported to GRAS and used as a sensitive volume for a beam or some other form of radiation source. The geometry made for the detector used in the present study is shown in the Figure 3.1, and the code is shown in Appendix A.

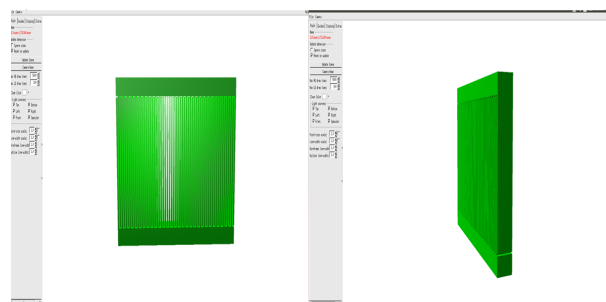


Figure 3.1: Detector geometry in ROOT's GL viewer, front (left) and side (right) view.

3.2.2 Monte-Carlo Simulations

In the present work, the Geant4 simulations are carried out using a set of macro commands provided from the GRAS toolkit. The corresponding macro file is shown in Appendix B, while the most important parts will be explained here. Initially the gdml geometry file is loaded:

```
/gras/geometry/type gdml  
/gdml/file Detector.gdml  
/gdml/setup world
```

Next, the physics lists are loaded as shown bellow with the example of a physics list regarding gamma nuclear reactions and stopping powers;

```
/gras/physics/addPhysics gamma_nuc  
/gras/physics/addPhysics stopping
```

These are used to define physical laws and rules in the simulations, which processes can occur and which particles can be used.

In GRAS/Geant4 the G4GeneralParticleSource (GPS) module is used for the specifications of spectral, angular and spatial distribution of particle sources. The neutron source was defined further as shown in the following lines:

```
/gps/particle neutron  
/gps/pos/type Point  
/gps/pos/centre 0.174 0 0.01 cm  
/gps/direction 0 0 -1  
/gps/ene/type Mono  
/gps/energy 14 MeV
```

Particles emitted by the source are neutrons with the energy 14 MeV, positioned at the center of the detector, and the direction given indicates that the source is emitting in the form of a beam. To visualize the created beam or source the following command is used:

```
/vis/scene/create  
/vis/open VRML2FILE
```

Next, the analysis module is added;

```
/gras/analysis/dose/addModule EdepInDiode1  
/gras/analysis/dose/EdepInDiode1/addVolume detector30_PV  
/gras/analysis/dose/EdepInDiode1/setUnit MeV
```

Lastly, a histogram is created;

```
/gras/histo/fileName kk
```

and the needed statistics defined:

```
/run/beamOn 1000000
```

The created source as well as the interaction with the detector geometry can be seen in Figure 3.2.

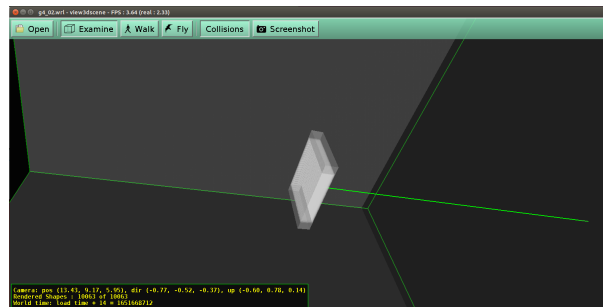


Figure 3.2: Detector geometry and neutron beam source.

3.2.3 Results

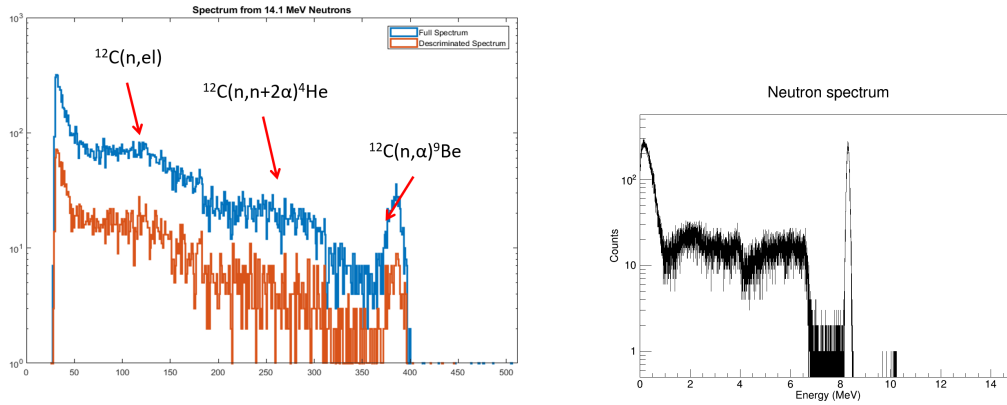
After the geometry and the source have been created their interaction can be simulated and visualized using ROOT. The analysis was made using ROOT Version 5.34/26 (Figure 3.3) data analysis framework developed in CERN and based on C++. The software allows the user to visualize large amounts of data and provides tools for data analysis. Analysis modules of GRAS include dose analysis, fluence



Figure 3.3: ROOT version 5.

analysis, Non Ionizing Energy Loss analysis (NIEL) etc. A number of simulations were made with the diamond detector geometry in Figure 3.1 and a gamma and neutron radiation source. The simulation results for neutrons were firstly compared

with the measured spectra which can be seen in Figure 3.4, (a) shows the measured spectrum for 14.1 MeV neutrons and (b) shows the simulated spectrum for 14 MeV neutrons.



(a) Measured spectrum for 14.1 MeV neutrons [6].

(b) Simulated spectrum for 14 MeV neutrons.

Figure 3.4: Simulated and measured spectra for neutrons.

The spectrum of gamma radiation from Americium-241 source can be seen in Figure 3.5. The simulation results for gamma rays with 3 MeV energy can be seen in

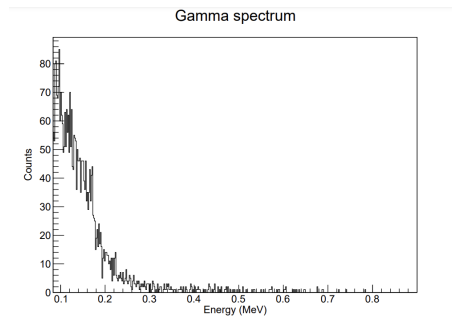
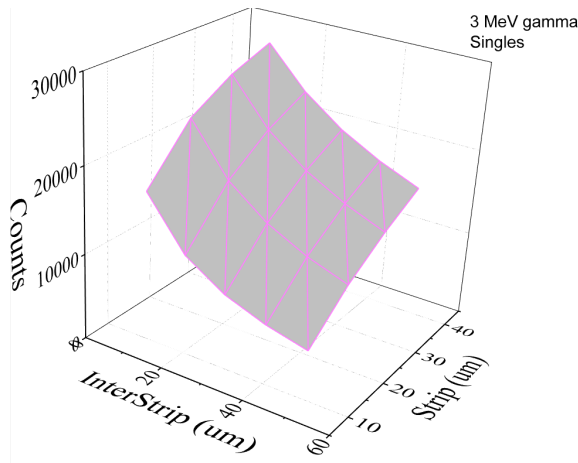
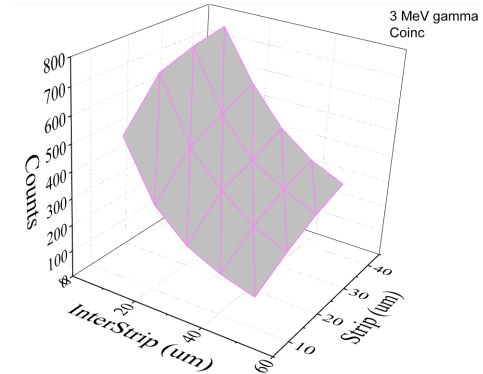


Figure 3.5: Simulation of gamma radiation spectrum made by Geant4.

Figure 3.6, with (a) being the results for singles mode, and (b) in coincidences mode. The same results can be seen in Figure 3.7 (a) and 3.7 (b) for neutrons with the energy 14.5 MeV. These simulations were used to determine the detector geometry needed. Taking a look at the position with the highest count for neutrons, and the lowest for gammas, strip width was determined to be $40 \mu m$ with the interstrip width of $20 \mu m$, but due to the limitations of the equipment used in the preparation of the detector this was changed to be $30 \mu m$ for both the interstrip and the strip width.

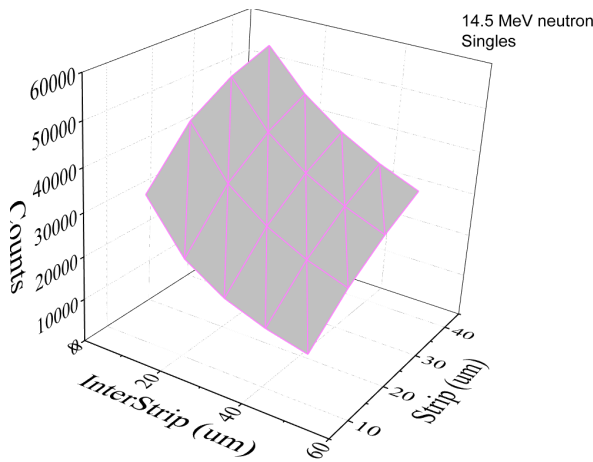


(a) Simulation results for 3 MeV gamma singles.

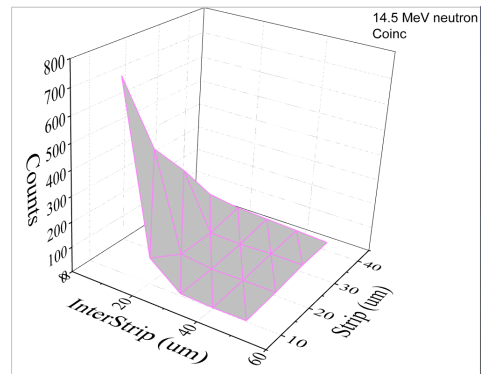


(b) Simulation results for 3 MeV gamma coincidences.

Figure 3.6: Simulations results for gamma rays in singles mode and coincidences mode.



(a) Simulation results for 14.5 MeV neutron singles.



(b) Simulation results for 14.5 MeV neutron coincidences.

Figure 3.7: Simulations results for neutron radiation in singles mode and coincidences mode.

3.3 SRIM Software Simulations

SRIM⁴ is the abbreviation for The Stopping and Range of Ions in Matter, and is a collection of software packages created by James F. Ziegler which has many uses regarding the transport of ions in matter (Figure 3.8).

Some of the applications are Ion stopping and range in targets, Ion implantation, Sputtering, Ion transmission and Ion beam therapy. SRIM can be used for calculations of stopping ranges or stopping powers of different ions in different materials as

⁴<http://www.srim.org/>

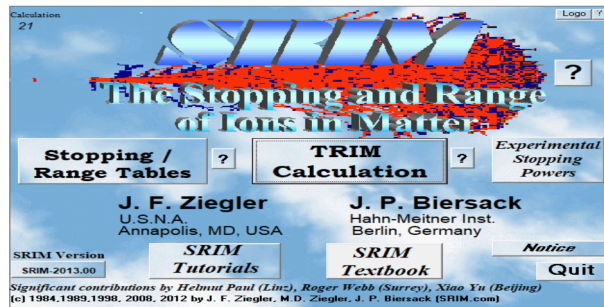
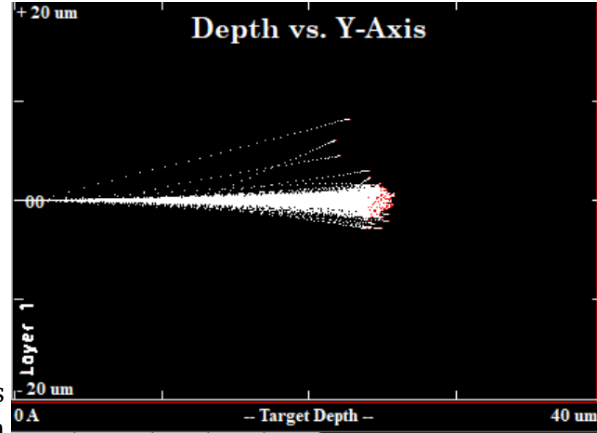


Figure 3.8: SRIM Software menu.

well as straggling distributions. The software allows the user to select an ion from the periodic table of elements and the energy of said ion, also the target can be chosen as well as its density. In this study SRIM was used to calculate stopping ranges of ions in materials and stopping powers, specifically the stopping range of protons in carbon with the density of diamond ($3,5 \text{ g/cm}^3$). The results table is shown in Figure 3.9 (a) for ion energies from 1 MeV to 5 MeV. Using this table one can now easily know which energy of the beam is needed for stopping in the material and which is needed for passing through it and if the beam passes through the material how much energy it has deposited per μm . It is obvious from the table that 2 MeV beam stops in the diamond (at approx. depth $24 \mu\text{m}$). Since the thickness of the used sample is $40 \mu\text{m}$, and the 3.5 MeV beam passes through the sample depositing $33.03 \text{ keV } \mu\text{m}$ energy the total deposited energy is 1.32 MeV. On the other hand, TRIM (The Transport of Ions in Matter) is a detailed Monte Carlo simulation based on phenomenological models for the interactions of ions with target atoms and electrons, for the determination of energy loss, angular straggling. The stopping ranges table uses preexisting parameters used with models for the combination of beam and target which the user inputs, and the results for the combination of a diamond target with thickness $40 \mu\text{m}$ and a proton beam with energy 2 MeV are shown in Figure 3.9 (a). Figure 3.9 (b) shows the ion distribution of hydrogen in carbon for given parameters.

Lastly, ionization profiles of 2 MeV and 3.5 MeV protons in diamond layer with thickness $40 \mu\text{m}$ were made and can be seen in Figure 3.10 (a) and Figure 3.10 (b). It is clear from these that protons with the energy 2 MeV deposit all their energy in diamond with the peak in Figure 3.10 (a) around $24 \mu\text{m}$ (as seen in Figure 3.9 (a)). Protons with energy 3.5 MeV on the other hand can be seen in Figure 3.10 (b) passing through the diamond depositing only a portion of their energy in the material

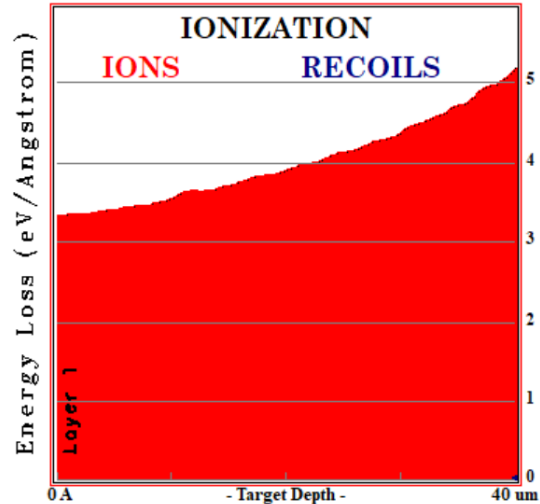
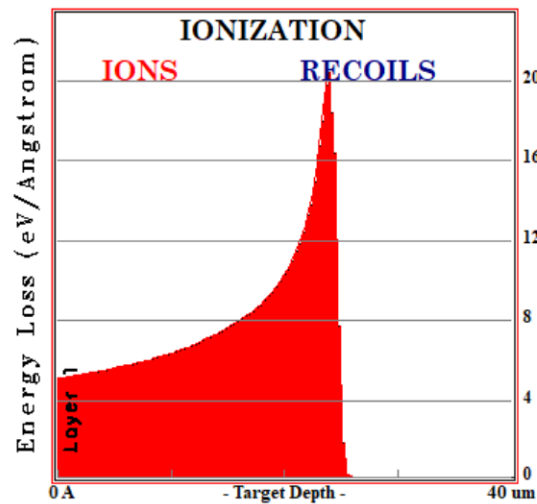
Ion Energy	dE/dx Elec.	dE/dx Nuclear	Projected Range	Longitudinal Stragging	Lateral Stragging
1.00 MeV	8.128E+01	5.360E-02	7.88 um	3398 A	2867 A
1.10 MeV	7.675E+01	4.934E-02	9.15 um	3895 A	3258 A
1.20 MeV	7.227E+01	4.574E-02	10.49 um	4390 A	3670 A
1.30 MeV	6.828E+01	4.266E-02	11.91 um	4890 A	4103 A
1.40 MeV	6.478E+01	3.998E-02	13.41 um	5396 A	4558 A
1.50 MeV	6.168E+01	3.764E-02	14.98 um	5909 A	5033 A
1.60 MeV	5.890E+01	3.557E-02	16.64 um	6428 A	5529 A
1.70 MeV	5.639E+01	3.373E-02	18.37 um	6955 A	6046 A
1.80 MeV	5.411E+01	3.208E-02	20.18 um	7489 A	6582 A
2.00 MeV	5.012E+01	2.924E-02	24.01 um	9392 A	7714 A
2.25 MeV	4.598E+01	2.636E-02	29.20 um	1.21 um	9236 A
2.50 MeV	4.254E+01	2.402E-02	34.85 um	1.47 um	1.09 um
2.75 MeV	3.962E+01	2.208E-02	40.92 um	1.72 um	1.26 um
3.00 MeV	3.712E+01	2.045E-02	47.43 um	1.97 um	1.45 um
3.25 MeV	3.494E+01	1.905E-02	54.36 um	2.23 um	1.65 um
3.50 MeV	3.303E+01	1.783E-02	61.70 um	2.48 um	1.86 um
3.75 MeV	3.134E+01	1.677E-02	69.46 um	2.74 um	2.07 um
4.00 MeV	2.982E+01	1.584E-02	77.62 um	3.00 um	2.30 um
4.50 MeV	2.723E+01	1.426E-02	95.13 um	3.94 um	2.79 um
5.00 MeV	2.509E+01	1.298E-02	114.22 um	4.83 um	3.32 um



(a) Stopping ranges and stopping powers of protons ($1\text{MeV} < E < 5\text{MeV}$) in carbon with thickness $3.5\text{g}/\text{cm}^3$ calculated using SRIM Software.

(b) Distribution of protons in carbon calculated using SRIM Software.

Figure 3.9: Stopping ranges, stopping power and proton distribution calculated using SRIM.



(a) Ionization profile for 2 MeV protons in diamond calculated using SRIM.

(b) Ionization profile for 3.5 MeV protons in diamond calculated using SRIM.

Figure 3.10: Ionization profile for protons in diamond calculated using SRIM.

(approx. 38% of the incident energy).

4 Experimental setup and method

4.1 *Diamond detector configuration*

4.1.1 Characteristics of the detector

The scCVD diamond crystal was purchased from Element Six⁵ and it is an electrical grade diamond. It is 4x4 mm in area and has the thickness of 40 μ m.

The diamond sample microscopic picture is shown in Figure 4.1. and Figure 4.2. Upon receiving the diamond samples, inspection was done using the microscope to see if any defects were visible. As seen in Figure 4.1. and Figure 4.2. there were some point and strain defects on the sample, but they were not considered problematic for further operation of the detector.



Figure 4.1: Microscopic picture of sample (right side).

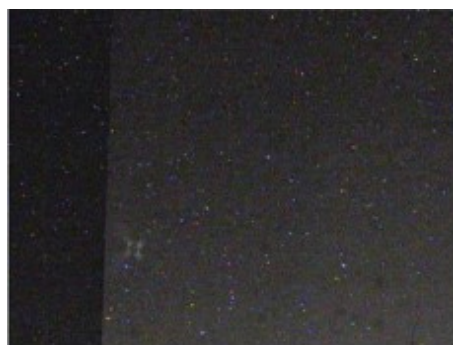


Figure 4.2: Microscopic picture of sample (left side).

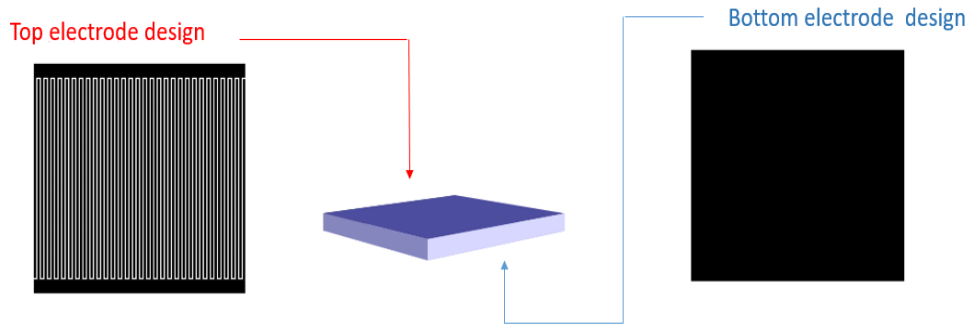


Figure 4.3: The design of the detectors top and bottom electrodes.

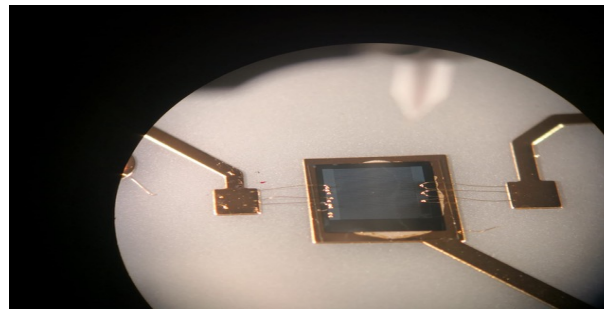


Figure 4.4: The sample after the pattern was deposited and wire bonding was made.

4.1.2 Construction of the detector

The sample was sent to the CEA LIST, Diamond sensors Laboratory for the electrode pattern to be made. The design of the detector can be seen in Figure 4.3. with the strip and interstrip width being $30 \mu m$, while the diamond with the pattern can be seen in Figure 4.4. The wire bonding was also made in the CEA LIST Laboratory and can also be seen in Figure 4.4. The electrodes were made of aluminum using standard contact photolithographic technique and the wire bonding of gold. The diamond was glued with silver paste onto the Printed Circuit Board (PCB) which was made of aluminum nitrate and designed in the Laboratory for ion beam interactions (RBI Zagreb). The board was then made by the company PCBONLINE⁶. The design of the PCB is shown in Figure 4.5. On the board four connectors can be seen, two for top electrodes of the diamond, one for the back electrode and one connector was made for temperature measurements which will be done in the future.

⁵<https://www.e6.com/>

⁶<https://www.pcbonline.com/>

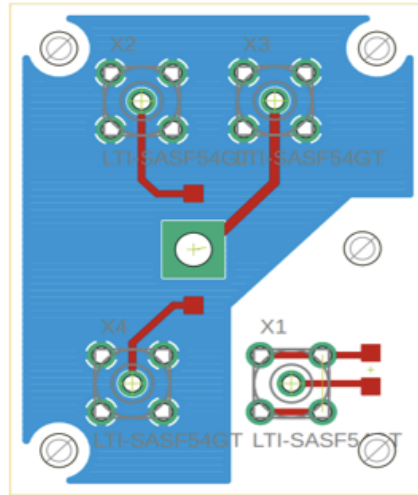


Figure 4.5: Printed circuit board design.

4.2 Experiment at the Laboratory for ion beam interactions

4.2.1 Particle accelerators

The experiment was conducted in the Laboratory for ion beam interactions at Rudjer Boskovic Institute in Zagreb. The laboratory is equipped with two particle accelerators, 6.0 MV EN Tandem Van de Graaf accelerator shown in Figure 4.6 on the left side and 1.0 MV Tandetron accelerator on the right side.



Figure 4.6: 6.0 MV EN Tandem Van de Graaf accelerator on the left and 1.0 MV Tandetron accelerator on the right.[5]

The 6.0 MV Tandem Van de Graaf accelerator works on the principle of Van de Graaf generator, which is an electrostatic generator. It uses a moving belt to create charge and accumulate it, creating a very high electric potential. In the case of the VDG accelerator, the potential created is positive and is used to accelerate negative ions from the ion source. The belt of the Van de Graaf generator is marked as 1 in Figure 4.7, further marked as 2 is the terminal of the VDG accelerator, under which

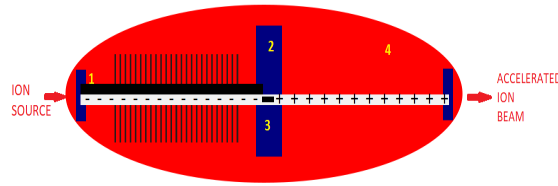


Figure 4.7: Scheme of the 6.0 Van de Graaf particle accelerator at LIBI.

marked as 3, the stripper gas is shown. The stripper gas is used for charge exchange, so the initially negative ions are stripped of electrons and positive ions are created. Stripper gas is Carbon dioxide (CO_2), but Nitrogen gas (N_2) can also be used. The accelerator works as a big pressure tank filled with insulation gas (4 in Figure 4.7), and the insulator gas used is Sulfur Hexafluoride (SF_6) and allows for a maximum voltage of 4 MV. The voltage used to create a proton beam of 2 MeV (like the one used in this experiment) is 1 MV, so negative ions are injected and then accelerated towards the terminal, and the positive ions are then again accelerated resulting in double energy. Depending on the charge state for heavier ions (e.g. oxygen), one can get energies up to 20-30 MeV. The ion source shown in Figure 4.8 is a sputtering negative ion source, because the accelerating voltage in VDG is positive. In the ion source there is a Cesium (Cs) vapor, which is ionized and accelerated towards the cathode, and it spatters ions from the cathode. The negative ions spattered are further accelerated and are guided to the first acceleration based on their mass using a magnet.

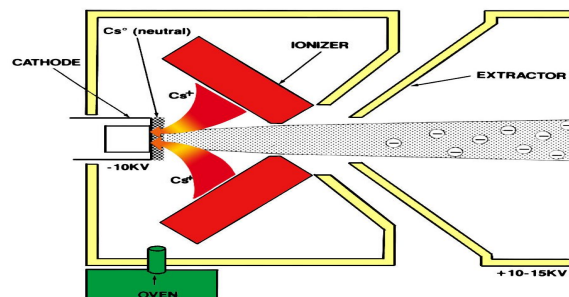


Figure 4.8: Scheme of the sputtering ion source.[9]

The second accelerator used in the experiment is the 1.0 MV Tandetron accelerator, shown in Figure 4.6 on the right with terminal voltages from 200 kV to 1

MV. It operates using two different ion sources, SNICS sputtering ion source and duoplasmatron ion source with Na charge exchange. The former was used for the experiment. In 1 MV Tandatron sputtering ion source is used for ion beams such as H, C, O, Si etc., while the duoplasmatron ion source is used mainly for ^3He and ^4He ion beams. The duoplasmatron ion source consists of three main parts, an anode, an intermediate electrode and a cathode. It operates using a gas which gets ionized in the chamber while interacting with electrons from the cathode forming a plasma. The plasma is further accelerated with sets of charged grids and forms an ion beam. The scheme of the duoplasmatron ion source can be seen in Figure 4.9. After the beam is accelerated it is transferred using a set of magnets to one of the experimental chambers. The magnet used for determining the energy of the beam is the analyzing magnet (90° magnet).

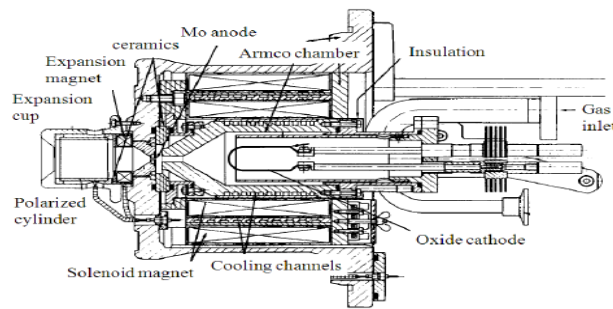


Figure 4.9: Scheme of the duoplasmatron ion source.[8]

The principle of energy determination is shown in Equation 4.1, and the scheme of the magnet is shown in Figure 4.10.

$$qvB = \frac{mv^2}{R} \quad (4.1)$$

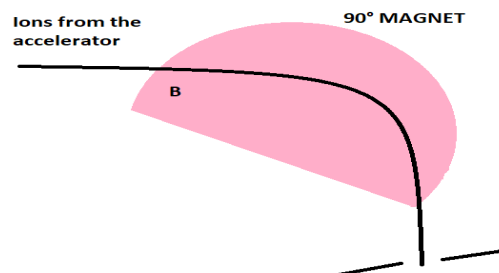


Figure 4.10: Scheme of the analyzing magnet.

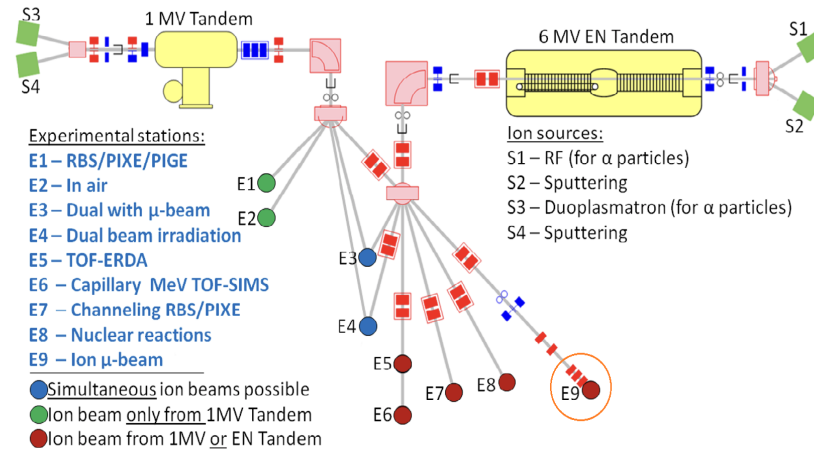


Figure 4.11: Experimental lines at the Laboratory for ion beam interactions. [5]

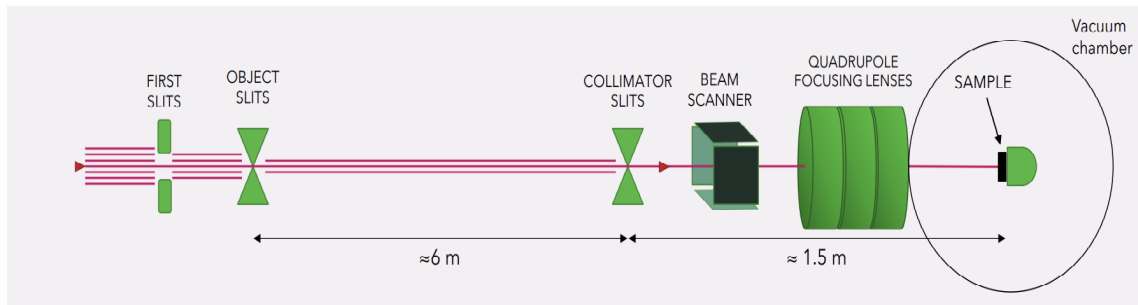


Figure 4.12: Illustration of an experimental line. Made by dr. sc. Andreo Crnjac.

As a charged particle (ion from the accelerator) is moving in a magnetic field the centripetal force is supplied by the magnetic force, and as the velocity of the particle is perpendicular to the magnetic field the magnetic force has a simplified form. Only the ions which pass through the slits in Figure 4.10 have the desired energy and are furthered transferred to the experimental chamber.

The laboratory has nine experimental lines as Figure 4.11 shows and the experiments for the characterization of the detector were carried out in in E9 and E3 which correspond to the ion microprobe and dual microprobe respectively. After the ions are accelerated the beam size is initially reduced using a set of slits and then focused using a triplet/doublet magnetic quadrupoles setup. In Figure 4.12 object slits and collimator slits used for focusing the beam are shown, as well as the beam scanner.

4.2.2 Ion microprobe

Nuclear microprobe is a setup that uses a system of quadrupole lenses (doublet or triplet) to focus an ion beam to micrometer size. The microprobe offers two operation

modes, with the current from 10 pA to a couple thousand pA and with the current being less than a few fA, so the setup offers the possibility to precisely control the beam current from a few fA up to nA and the beam spot from 200 nm up to a few mm. In the Laboratory for ion beam interactions (LIBI) both microprobes are equipped with appropriate setups for material analysis studies, i.e. PIXE, RBS, NRA, PIGE, STIM, IBIC as well as materials irradiations and modifications. The detector response was studied by means of the IBIC technique. Scanning speed offered in the microprobe is from 100 ms to 10 ms per pixel, while the sample movement ranges are 100 mm in the x direction and 25 mm in both y and z directions. The sample with maximum possible dimensions 60 mm x 30 mm x 10 mm can be tilted for 360° continuously around the x axis. Two microprobe chambers were used in this paper, the ion microprobe (experimental line E9 in Figure 4.11) and the dual microprobe (experimental line E3 in Figure 4.11) where the beams from both accelerators can simultaneously be focused.

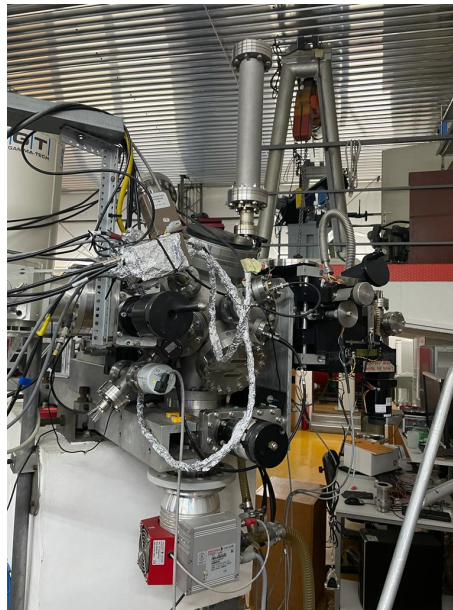


Figure 4.13: The experimental line E9 - ion microprobe.

The interior of both microprobe chambers is similar and can be seen in Figure 4.15 with STIM detectors, germanium detectors, PIXE detectors and RBS/NRA detectors as well as the Piezzo stages for mounting and precise positioning of the samples. The dual microprobe's stage as opposed to ion microprobe's doesn't have the option of rotation of sample in such range.

The beam is rastered over the samples surface by the scanner shown in Figure

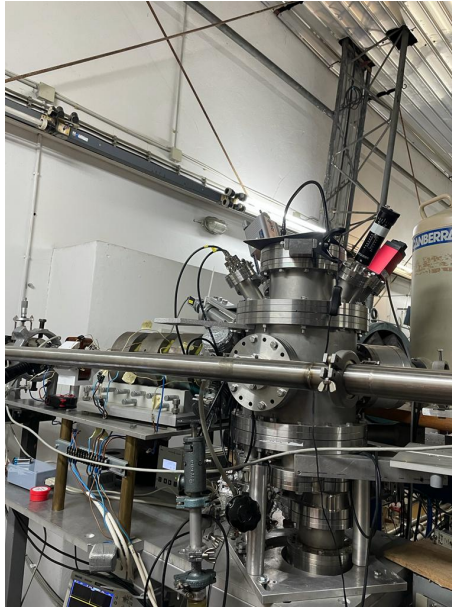


Figure 4.14: The experimental line E9 - dual microprobe.

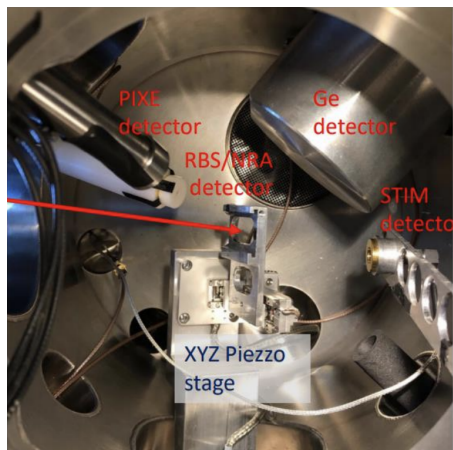


Figure 4.15: The inside setup of the ion microprobe chamber.

4.12 and different scanning options may be seen in Figure 4.16.

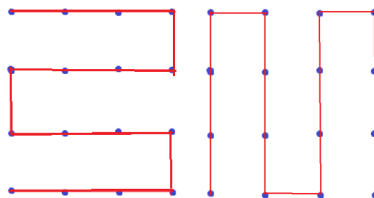


Figure 4.16: Beam scanning options.

4.2.3 Ion Beam Induced Charge Microscopy (IBIC)

For the application of Ion beam Induced Charge Microscopy (IBIC) a current of few fA, corresponding to a beam particles frequency of few kHz is sufficient. An ion traversing through a material creates ionization along its trajectory. In a semiconductor, those charges, corresponding to electrons and holes, can drift by applying an electric field. This movement induces a signal at the electrodes. The ion position is correlated with pulse height and images of charge collection properties are obtained.

4.2.4 Scanning Transmission Ion Microscopy (STIM)

Scanning transmission ion microscopy (STIM) is a technique used to detect transmitted ions, most often protons or alpha particles. The way in which the particle loses energy in the sample provides information about the density and structure of the sample, and is used to map the structure of the thin samples (up to 30 μm). Energy loss of ions transmitted through a sample depends on the sample's areal density (A) which could be defined as [23, p. 173]:

$$A = \int_{InitialEnergy}^{RemainingEnergy} \left(\frac{dE}{d(\rho z)} \right)^{-1} dE \quad (4.2)$$

Using a semiconductor detector (e.g. surface barrier detector) positioned behind a sample transmitted ion energies and number of ions at every pixel of the scanned area are measured. This technique was used for scanning the copper mesh grids in order to determine the focused beam spot dimensions and the real scan sizes in IBIC maps.

4.2.5 Data acquisition and the electronic chain

The data acquisition system in LIBI consists of hardware and software components. The typical electronic chain can be seen in Figure 4.17, it consists of the diamond detector (or any other detector for ionizing radiation), very close to the detector is then the charge sensitive preamplifier which outputs a pulse of few mV, proportional to the collected charge from the detector's electrodes.

The shaping amplifier further amplifies the signal to a few volts and shapes it. Pulse height analysis is then performed by the Analog to Digital Converter (ADC)

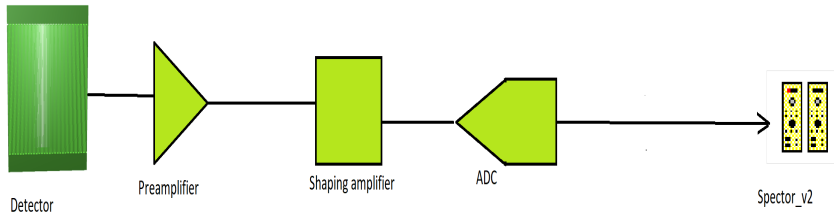


Figure 4.17: The electronic chain used for data acquisition.

and the pulse processing is then done digitally and histograms can be collected using Spector_v2 software. In this experiment the amplifiers used were Ortec 570, Canberra 2022 and Ortec 572 and the ADCs used were Canberra Fast ADC 8075 and 8077. These can be seen in Figure 4.18. Spector_2 is a software created and used

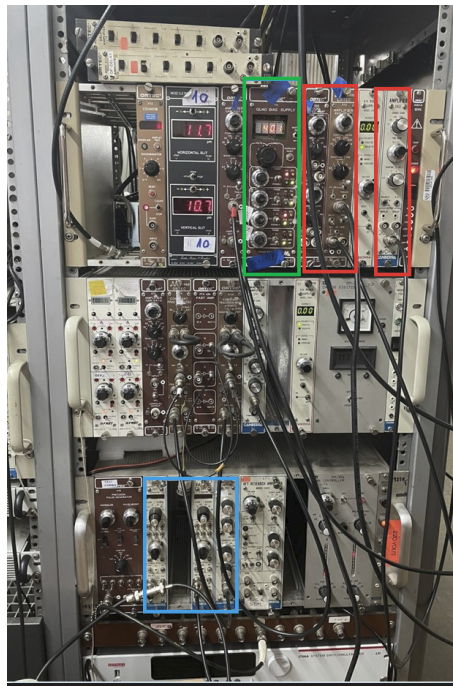


Figure 4.18: The setup used for measurement in experimental line E9 with proton beam energies 2 MeV and 3.5 MeV. The green marks the Ortec 710 Quad 1 kV Bias Supply, the blue marks the ADCs and the red the amplifiers used.

in the Laboratory for ion beams interactions for data acquisition, it is used to save histograms as .LST and .DAT files which allows the user to replay measurements and process data easily.

4.2.6 Experimental setup and procedures

Proton beams with energies 2 MeV and 3.5 MeV were accelerated using the Tandem Van de Graaf accelerator and with the set of magnets was guided to the experimental line E9 which is the ion microprobe (Figure 4.13).

The detectors used in these measurements is the STIM detector (can be seen on the right side of Figure 4.15) which is a surface barrier detector used for images of the mesh grid. The diamond detector was mounted on the piezzo stage, this configuration can be seen in Figure 4.19. Three amplifiers (Ortec 570, Canberra 2022 and

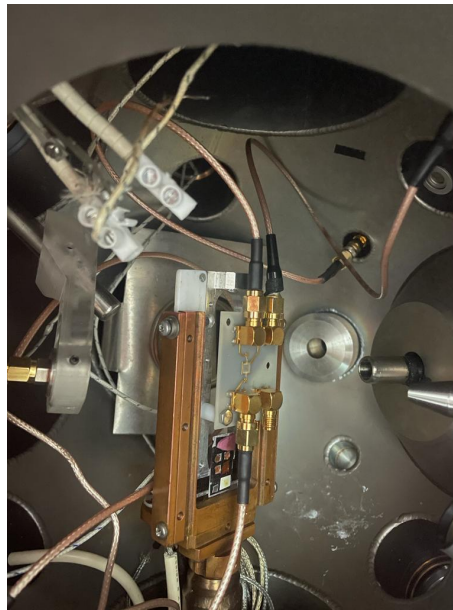


Figure 4.19: Setup with the diamond detector in the ion microprobe chamber on experimental line E9.

Ortec 572), preamplifiers and analog to digital converters - ADCs (Canberra Fast ADC 8075 and 8077) were used as well as the electronic chain for STIM measurements. Each electrode was connected to a separate preamplifier, amplifier and ADC and a computer software Spector_v2 was used for data collection. It can be seen in Figure 4.19 that one connector on the PCB is not connected to the electronic chain and this is the connector for future temperature measurements as this detector has the potential to work on very high/low temperatures. A similar setup was used for the single mode experiments conducted in the dual microprobe chamber (experimental line E3), with the proton beams of 1 MeV and 2 MeV accelerated using the Tandetron accelerator (Figure 4.20 and Figure 4.14). The general setup is also the same for the coincidences measurement with the 1.8 MeV proton beam from the Tandetron accel-

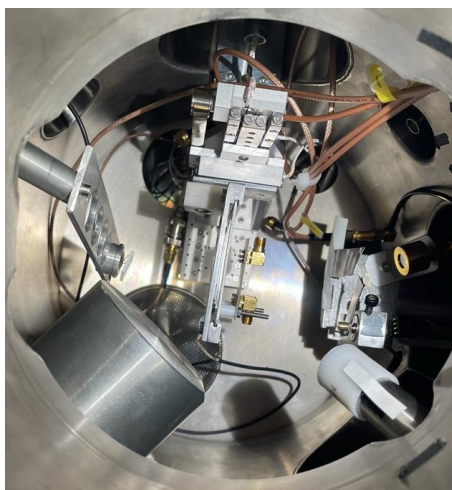


Figure 4.20: Setup with the diamond detector in the dual ion microprobe chamber on experimental line E3.

erator and alpha radiation source except for the electronic chain which was discussed in Section 4.2.5. When using the radiation sources the detector was still mounted to the piezzo stage of the microprobe chamber and placed in vacuum with the source placed close to it, at the distance of 2-3 cm.

4.3 Experiments in coincidence mode

The electronic chain for coincidences measurement is somewhat different then the measurement in single mode as it also contains a gate and delay generator as well as a delay amplifier. The delay amplifier used was Ortec Model 427 A⁷ and it can be used to delay linear or logical signals with the delay range of 0-4.75 μs . The gate and delay generator used was a Ortec Model 416 A Gate & Delay Generator⁸ and it adjusts delay, width, polarity and amplitude of pulses with the delay of 0.1 to 110 ns. The amplifiers used were Canberra Spectroscopy Amplifier Model 2020, Canberra Amplifier 2026⁹ and Ortec 672 Spectroscopy Amplifier, while the analog to digital converters used were Canberra ADC 8075. The setup can be seen in Figure 4.21. The gate and delay generator was used here to delay a signal coming from one electrode and create a window which is then triggered by the signal from the other electrode. The scheme of the electronic chain in coincidence mode can be seen in

⁷<https://www.ortec-online.com/products/electronics/amplifiers/427a>

⁸<https://www.ortec-online.com/products/electronics/delays-gates-and-logic-modules/416a>

⁹<https://www.mirion.com/>

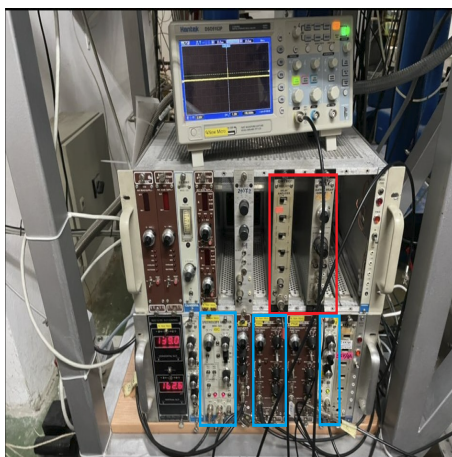


Figure 4.21: Setup used for coincidence measurement, red marks the delay amplifier Ortec Model 427 A and Ortec Model 416 A Gate & Delay Generator, while the blue marks the amplifiers used: Canberra Spectroscopy Amplifier Model 2020, Canberra Amplifier 2026 and Ortec 672 Spectroscopy Amplifier.

Figure 4.22.

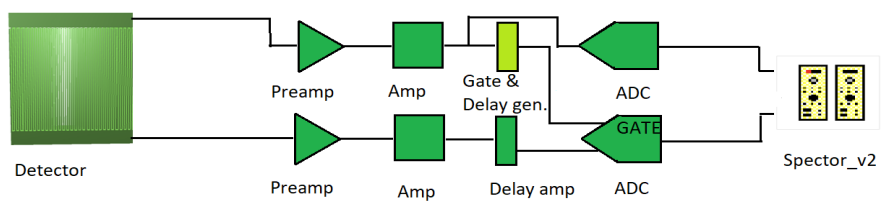
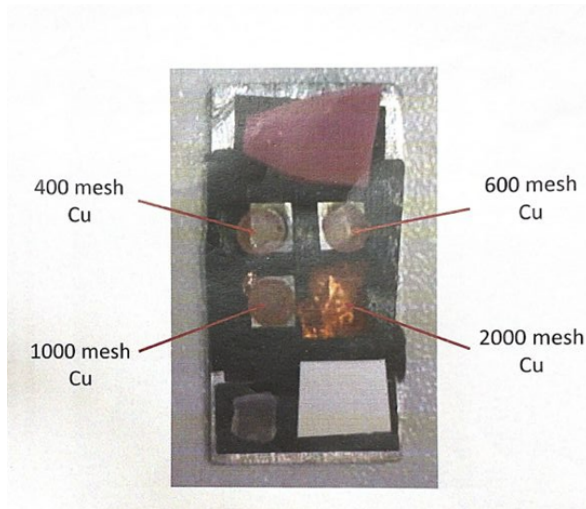
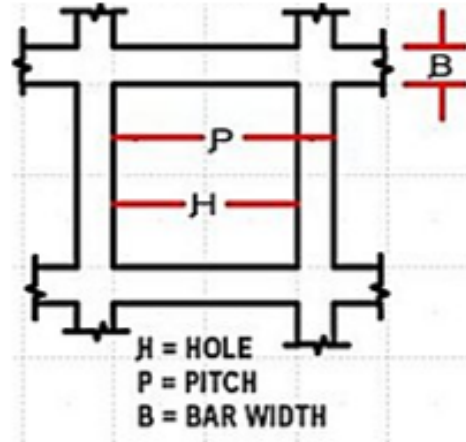


Figure 4.22: Electronic chain for coincidence measurement.



(a) Set of grids used for real size calculation and quartz used for focusing the beam.



(b) One cell of a mesh grid.

Figure 5.1: Set of grids used (a) and one cell of a mesh grid (b).

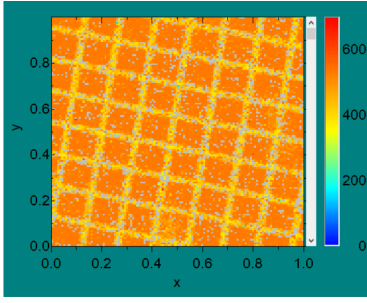
5 Results and discussion

Initially the ion beam was focused using the scintillation light emitted from a quartz. Then, in order to estimate the beam spot and adjust the scan size, several grids were used. They were made out of copper and were 400, 600, 1000 and 2000 SPI mesh grids. In Figure 5.1 (a) in addition to the grids, the quartz, a scintillator and a Gadolinium Oxysulfide scintillator screen used for focusing the beam, can be seen. The 400 mesh grid was used for calculating the map pixel size in μm . The scanned grid can be seen in Figure 5.2 (a) for a proton beam with energy 2 MeV and scan size 2x1, and in Figure 5.2 (b) for a proton beam with energy 3.5 MeV and scan size 1.25x1.

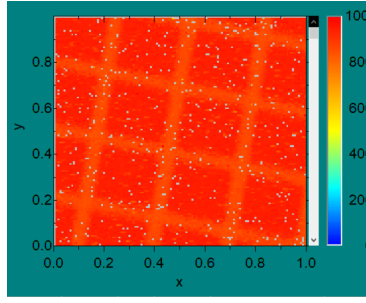
Mesh	400	600	1000	2000
Pitch (μm)	62	42	25	12.5
Bar width (μm)	16	5	6	5
Hole width (μm)	46	37	19	7.5

Table 5.1: Table of 400, 600, 1000, 2000 copper mesh grids' properties

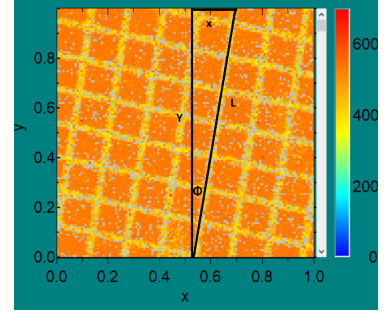
The real pixel size is calculated using the known size of the bar and hole of the grid which are for the 400 mesh grid 16 μm for the bar and 46 μm for the hole. Taking a look now at the collected grid in Figure 5.2 (c) the process of real pixel size can be explained. Using the hole and bar sizes for the 400 mesh grid length L in



(a) 400 mesh grid scanned using a proton beam with energy 2 MeV and scan size 2x1.



(b) 400 mesh grid scanned using a proton beam with energy 3.5 MeV and scan size 1.25x1.



(c) 400 mesh grid scanned using a 2MeV proton beam and scan size 2x1 with geometry for real pixel size calculation.

Figure 5.2: IBIC images of 400 mesh grid and geometry used for calculation of real pixel size.

Figure 5.2 (c) can be calculated as:

$$L = 7.4 \cdot H + 8 \cdot B = 7.4 \cdot 46\mu m + 8 \cdot 16\mu m = 468.4\mu m \quad (5.1)$$

The dimensions of the maps are 128x128 pixels. Using basic trigonometry the angle $\tan(\phi)$ can be obtained and from it $\cos(\phi)$:

$$\cos(\phi) = \cos(\arctan(\frac{x}{128})) = 0.9854 \quad (5.2)$$

where x is approximated as 22.1 px using the dimensions of the map. Now the real height of the map can be calculated as:

$$Y = 0.9854 \cdot L = 461.56\mu m \quad (5.3)$$

and by dividing this result by 128 the real pixel size for scan size 2x1 is $3.6 \mu m/px$. Dividing this result by two the real pixel size is obtained for 2 MeV energy protons and scan size 1x1 as $\Delta p = 1.8\mu m/px$. This procedure can be done now also for the scanned grid with energy 3.5 MeV and for scan size 1.25x1 and overall result with pixel sizes normalized to scan size 1x1 are shown in Table 5.1. The average pixel size is then $1.75 \mu m$.

After calculating real pixel size for both scan sizes the measurement with the diamond detector was conducted. Using the proton beam with energy 2 MeV IBIC

Energy (MeV)	2	3.5
Real pixel size(μm)	1.8	1.7

Table 5.2: Real pixel size results for energies 2 MeV and 3.5 MeV.

maps were obtained. In Figure 5.3 IBIC images of both top electrodes can be seen, both with bias voltages 1 V and no leakage current on any electrode. In Figure 5.4

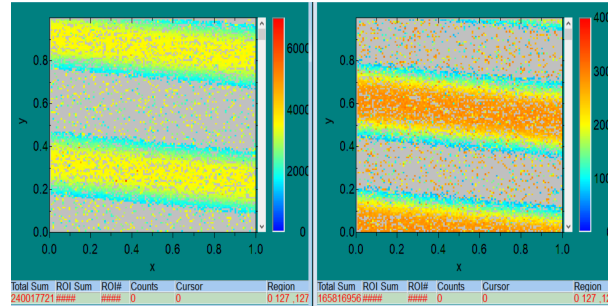
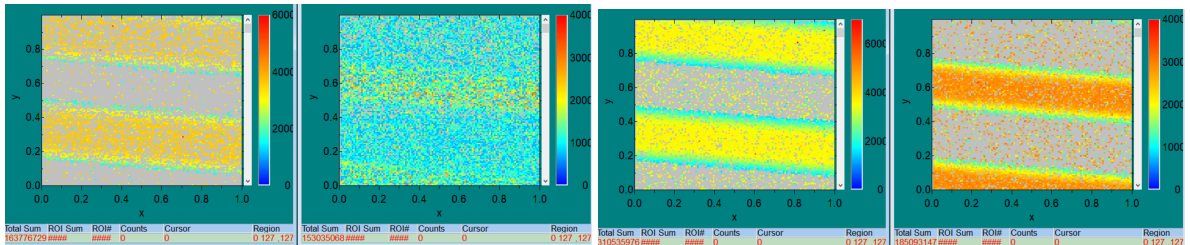


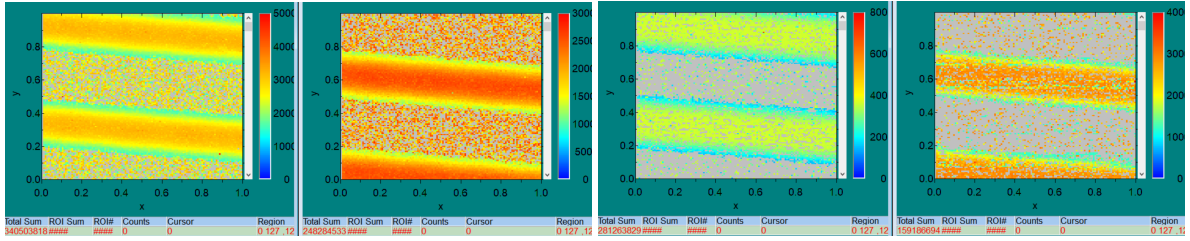
Figure 5.3: IBIC images of top electrodes with bias voltage 1 V.

(a) voltage was increased to 5 V on both top electrodes with the leakage current on one being $0.02 \mu A$. In this case one can observe that the two electrodes are not symmetrical, and on the right-hand side there is a lot of noise visible because of the leakage current. In Figure 5.4 (b) one of the top electrodes was put on bias voltage 5 V with the leakage current $0.02 \mu A$ and the other was put on bias voltage 3 V. Now as the resulting voltages are same on both electrodes IBIC images of the top electrodes are symmetrically wide. So far the polarity of the voltage on top electrodes was positive and the next step was changing it to negative. In Figures 5.5 (a), 5.5 (b) and 5.6 (a) and 5.6 (b) the corresponding IBIC maps are shown. In Figure 5.5 (a) voltage on both electrodes is -1 V with no leakage current, and in Figure 5.5 (b) bias



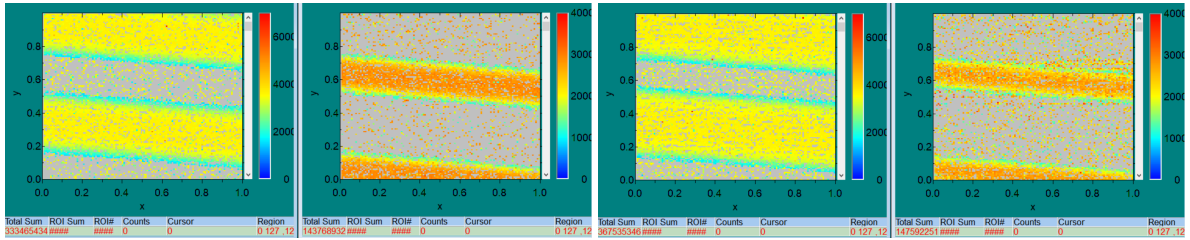
(a) IBIC images of top electrodes with bias (b) IBIC images of top electrodes with bias voltage 5 V. voltage 5 V and 3 V.

Figure 5.4: IBIC images of both top electrodes at positive voltages probed using a proton beam with 2 MeV energy.



(a) IBIC images of top electrodes with bias voltage -1 V. (b) IBIC images of top electrodes with bias voltage -3 V.

Figure 5.5: IBIC images of both top electrodes at negative voltages (-1 V and -3 V).



(a) IBIC images of top electrodes with bias voltage -5 V. (b) IBIC images of top electrodes with bias voltage -9 V.

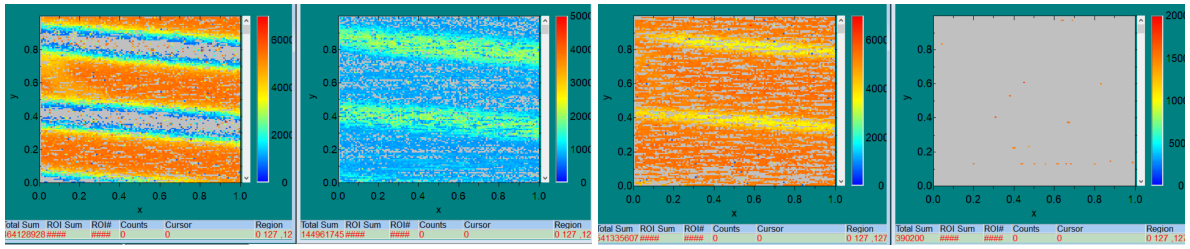
Figure 5.6: IBIC images of both top electrodes at negative voltages (-5 V and -9 V).

voltage on both top electrodes is -3 V also with zero leakage current. It is important to note that the bias voltage on the back electrode is zero.

On higher voltages than ± 3 V leakage current is noticeable as well as noise. The deterioration of IBIC image quality of electrodes is visible in Figure 5.6 (a) and 5.6 (b) where voltages on top electrodes are -5 V and -9 V with leakage current being $0.02 \mu A$ and $0.06 \mu A$ respectively.

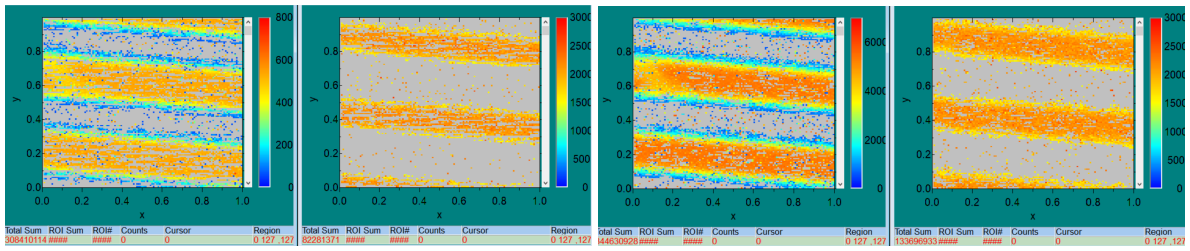
After changing the energy of the proton beam from 2 MeV to 3.5 MeV similar measurements were done, positive and negative voltages were applied to top electrodes of the detector and IBIC images were obtained. It is important to note that the proton beam with the energy 2 MeV deposits all energy in the detector material, while the proton beam of 3.5 MeV energy passes through and deposits only a portion of its energy in the detector material. In Figure 5.7 (a) voltage -5 V was applied to both top electrodes, and signals were taken from both top electrodes. Leakage current on one of the top electrodes is still present and in this case it is $0.02 \mu A$.

Further, even higher voltage (-20 V) was applied to the top electrode which has so far shown no leakage current and the voltage on the other was kept at -5 V. The resulting IBIC image is shown in Figure 5.7 (b). The polarity of the voltages is now changed, and Figures 5.8 (a) and 5.8 (b) show the top electrodes with positive bias



(a) IBIC images of top electrodes with bias (b) IBIC images of top electrodes with one voltage -5 V. electrode at -20 V, and the other at -5 V.

Figure 5.7: IBIC images of both top electrodes at negative voltages probed using a proton beam with 3.5 MeV energy.



(a) IBIC images of top electrodes with both (b) IBIC images of top electrodes with one electrodes at 5V. electrode at 3 V, and the other at 5 V.

Figure 5.8: IBIC images of both top electrodes at positive voltages probed using a proton beam with 3.5 MeV energy.

voltage applied, Figure 5.8 (a) with both electrodes at 5 V, and Figure 5.8 (b) with 3 V and 5 V on the electrodes. Leakage on one electrode is still zero and the other $0.02 \mu A$.

In order to simulate gamma radiation detector response, the sample was tilted by 10 degree steps with the bias voltage on the back electrode being -40.1 V until overlap between electrodes' signals was noticed corresponding to ions transversing through both the sensitive volumes formed from the two electrodes. This overlap is shown in Figure 5.9 where the sample was rotated by 65 degrees. Using the IBIC images

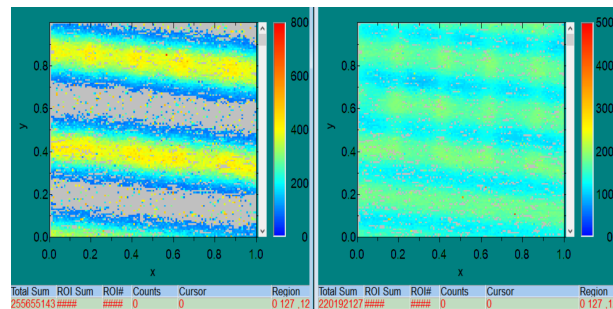
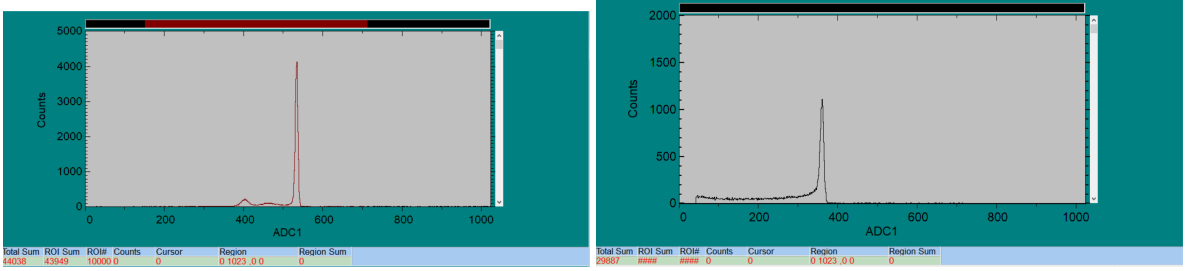


Figure 5.9: IBIC image of both electrodes with the back electrode at -40.1 V and the sample tilted by 65 degrees.



(a) The spectrum taken with the STIM detector with voltage applied 55 V and 2MeV proton beam. (b) The spectrum taken with the diamond detector with voltage applied 3 V and 2MeV proton beam.

Figure 5.10: Spectrums used for CCE calculation.

collected as well as the pulse height of the STIM detector, charge collection efficiency curves were made for all three electrodes. Using the peak channel collected with the STIM detector which can be seen in Figure 5.10 (a) and the peak channel collected with the diamond detector which can be seen in Figure 5.10 (b), the amplification (gain) and the number of electron-hole pairs created in silicon and diamond with the energy of the beam the CCE for the diamond detector can be obtained. The formula used is:

$$CCE_{Diamond} = 100\% \cdot \frac{A_{Diamond}G_{Si}B_{Si}}{A_{Si}G_{Diamond}B_{Diamond}} \quad (5.4)$$

where A is the peak channel for silicon or diamond, G is the amplification and B is the number of electron-hole pairs created in diamond or silicon and the values of B are calculated as follows:

$$B = \frac{E}{w} \quad (5.5)$$

In the Table 5.2 number of electron-hole pairs created for silicon and diamond are shown for energies 2 MeV and 3.5 MeV. Charge collection efficiency graph for the top

Element	Silicon	Diamond	Silicon	Diamond
Energy (MeV)	2	2	3.5	1.3
w-value (eV)	3.62	13	3.62	13
Number of e-h pairs	552,486.2	153,846.2	966,850.8	101,538.5

Table 5.3: Table of electron-hole pairs created in silicon and diamond for two energies.

electrode of the diamond detector which showed no leakage in this measurement for beam energy 2 MeV can be seen in Figure 5.11, the shape of the graph is expected

and the plateau is reached between 6 to 8 volts. The similar procedure was done

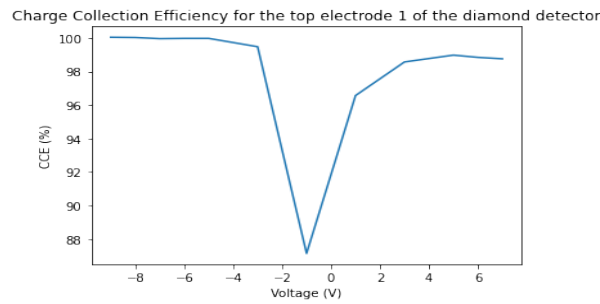


Figure 5.11: CCE graph for the top electrode with no leakage current, beam energy is 2 MeV.

for the second top electrode with the Channel-Voltage graph shown in Figure 5.12. When applying higher voltage to an electrode, the strip width of that electrode in the

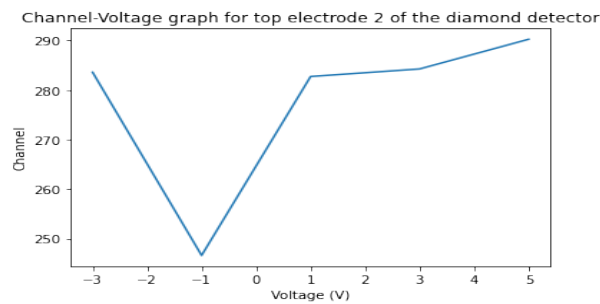


Figure 5.12: Channel-Voltage graph for the top electrode with leakage current, beam energy is 2 MeV.

IBIC images expands because of stronger electric field. This is shown in Figure 5.13 as the red shaded area corresponds to the nominal strip width of 30 μm it can be seen that with voltage applied this width expands, and it expands more for higher voltages.

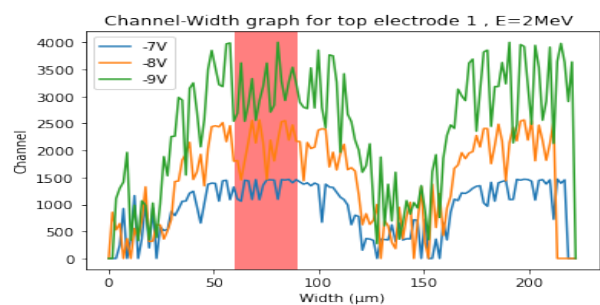
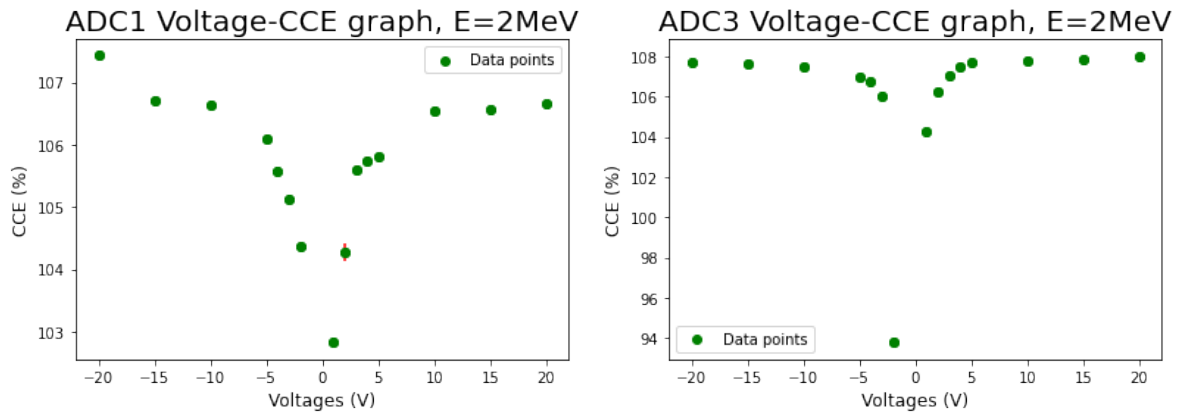


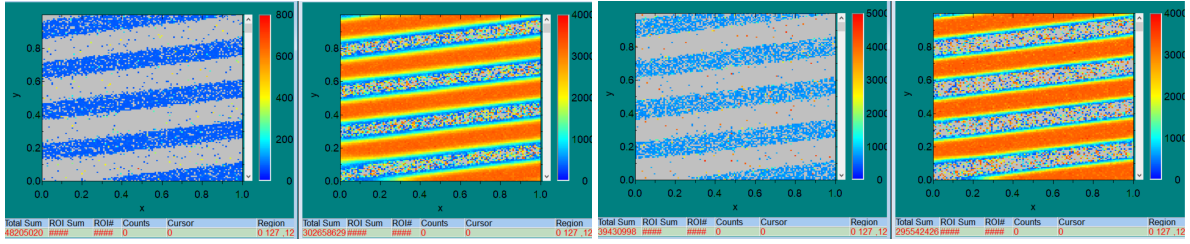
Figure 5.13: Channel-width graph for the top electrode 1 with no leakage current, beam energy is 2 MeV.



(a) CCE-Voltage graph for one top electrode (b) CCE-Voltage graph for the second top electrode connected to ADC1 probed with the 2 MeV proton beam. (c) CCE-Voltage graph for the second top electrode connected to ADC3 probed with the 2 MeV proton beam.

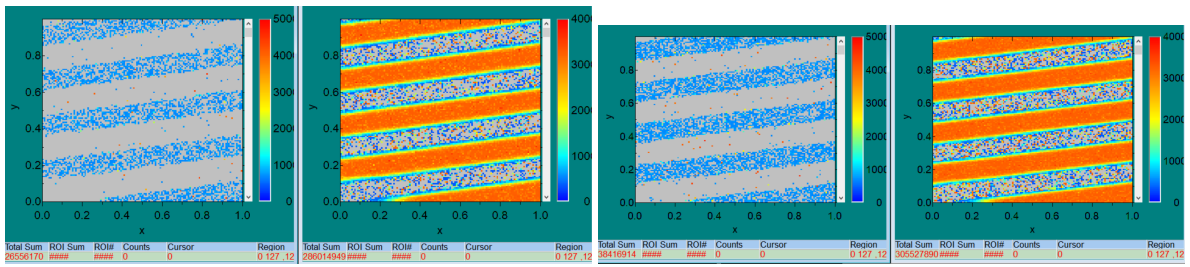
Figure 5.14: CCE-Voltage graph for the top electrodes of the detector.

The measurement with proton beam energies 2 MeV and 1.8 MeV from Tandatron accelerator were made after cleaning the sample using EM-KLEEN Plasma Cleaner. With the 2 MeV beam single mode measurement was conducted and with the 1.8 MeV proton beam the coincidences measurement was conducted. The noise in the setup of the previous measurement was proven to be caused by the electronics, as in this setup the noise was minimal and the electrodes could be put to much higher voltages. The results of measurements in single mode with the 2 MeV proton beam are shown as CCE-Voltage curves in Figure 5.14, on the left side (5.14 (a)) for one top electrode and on the right side (5.14 (b)) for the other top electrode. Lastly, coincidences measurements were conducted using a 1.8 MeV proton beam. One electrode creates the gate while on the other single events are observed. The results with both electrodes at same voltages can be seen in Figure 5.15 and Figure 5.16. In Figure 5.15 (a) the applied voltage on both electrodes was 5 V, while in 5.15 (b) applied voltage was 10 V. The left maps show the coincidences on one electrode, while the right show single events on the other electrode. Figure 5.16 shows the same, but the voltages applied on both electrodes were 15 V in Figure 5.16 (a) and 25 V in Figure 5.16 (b). It can be seen that there are some events visible outside the coincidence area, these are random events caused by the noise. There seems to be more of these events on lower and positive voltages. By changing the scan size a better insight into the coincidence area was obtained. This can be seen in Figure 5.17 (a) for scan size 0.5, and in Figure 5.17 (b) for scan size 4, in both cases the voltage



(a) IBIC maps for coincidence measurements with both electrodes at 5 V. (b) IBIC maps for coincidence measurements with both electrodes at 10 V.

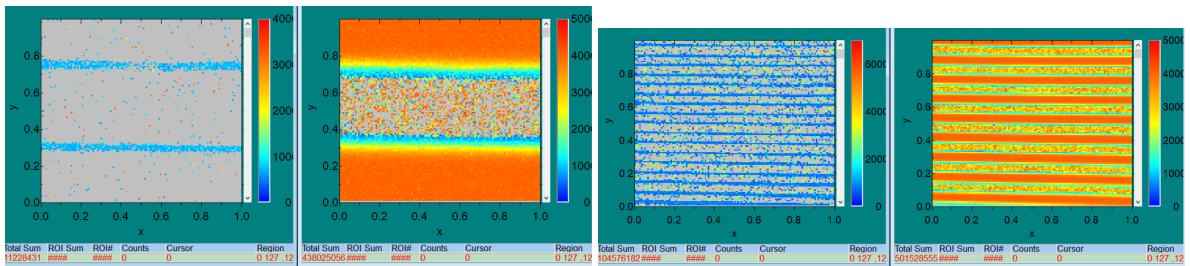
Figure 5.15: IBIC maps for coincidence measurements.



(a) IBIC maps for coincidence measurements with both electrodes at 15 V. (b) IBIC maps for coincidence measurements with both electrodes at 25 V.

Figure 5.16: IBIC maps for coincidence measurements.

applied on both electrodes was -10 V, and here the energy of the proton beam is 2 MeV. The coincidence area width was calculated from the map in Figure 5.17 (a) and it is $6.2 \pm 0.5 \mu m$.



(a) IBIC maps for coincidence measurements with both electrodes at -10 V and scan size 0.5. (b) IBIC maps for coincidence measurements with both electrodes at -10 V and scan size 4.

Figure 5.17: IBIC maps for coincidence measurements with different scan sizes.

6 Summary and outlook

6.1 Summary

In this paper a new detector configuration for discrimination of neutron and gamma radiation was introduced, developed and tested. The properties of this new detector were probed by means of the IBIC technique using proton beams with energies 1.8, 2 and 3.5 MeV, as measurements in single and coincidence mode were conducted. Initially, increased leakage current was observed in one electrode as such the corresponding CCE was not 100%. In order to solve this the detector was cleaned using the EM-KLEEN Plasma Cleaner and moreover the electronic chain was fine tuned. The experiment was repeated in the dual microprobe chamber where good functionality of both electrodes was observed with high signal to noise ratio and 100% charge collection efficiency. With this improved setup the coincidence measurement was carried out. The latter showed that the two electrodes operate as independent detectors and it is planned to be used for the discrimination of fast neutrons and gamma rays.

6.2 Outlook

The next step in working with this detector is to investigate its performance in a mixed neutron and gamma environment, i.e. RBI Neutron generator. Moreover, high and low temperature measurements are planned to be conducted in the future to confirm the detectors good performance under harsh conditions.

Appendices

Appendix A Detector geometry .c file

```
void Detector()
double dumm = 180;

    double length = 0.0015;
double width = 0.144;
double thick = 0.03;
double C_Density=3.5;
double width2 = 0.02;

    gSystem->Load("libGeom");
TGeoManager *geom = new TGeoManager("C-Crystal", "C Geometry");

    TGeoMaterial *matVacuum = new TGeoMaterial("Vacuum",1.01,1,1.e-25,TGeoMaterial:
:kMatStateGas,2.73,3.0e-18);

    TGeoElementTable *table = new TGeoElementTable(200);
TGeoElement *carbon = table->FindElement("C");

    TGeoMaterial *matDiamond = new TGeoMaterial("Carb", carbon,3.5);
matDiamond->SetState(TGeoMaterial::kMatStateSolid);

    TGeoMedium *Vacuum = new TGeoMedium("Vacuum",7, matVacuum);
TGeoMedium *Diamond = new TGeoMedium("Diamond",6, matDiamond);
TGeoTranslation *center_of_container = new TGeoTranslation("center_of_container",0.,0.,0);
center_of_container->RegisterYourself();

    TGeoRotation rot1;
rot1.RotateY(0);
rot1.RotateX(0);
```



```

rot1.RegisterYourself();
TGeoTranslation *tr17 = new TGeoTranslation("tr17",0,length,0);
TGeoTranslation *tr18 = new TGeoTranslation("tr18", length*3,0,0);
TGeoTranslation *tr19 = new TGeoTranslation("tr19", length*6,length,0);
TGeoTranslation *tr20 = new TGeoTranslation("tr20",length*9,0,0);
TGeoTranslation *tr21 = new TGeoTranslation("tr21",length*12,length,0);
TGeoTranslation *tr22 = new TGeoTranslation("tr22",length*15,0,0);
TGeoTranslation *tr23 = new TGeoTranslation("tr23",length*18,length,0);
TGeoTranslation *tr24 = new TGeoTranslation("tr24",length*21,0,0);
TGeoTranslation *tr25 = new TGeoTranslation("tr25",length*24,length,0);
TGeoTranslation *tr26 = new TGeoTranslation("tr26",length*27,0,0);
TGeoTranslation *tr27 = new TGeoTranslation("tr27",length*30,length,0);
TGeoTranslation *tr28 = new TGeoTranslation("tr28",length*33,0,0);
TGeoTranslation *tr29 = new TGeoTranslation("tr29",length*36,length,0);
TGeoTranslation *tr30 = new TGeoTranslation("tr30",length*39,0,0);
TGeoTranslation *tr31 = new TGeoTranslation("tr31",length*42,length,0);
TGeoTranslation *tr32 = new TGeoTranslation("tr32",length*45,0,0);
TGeoTranslation *tr33 = new TGeoTranslation("tr33",length*48,length,0);
TGeoTranslation *tr34 = new TGeoTranslation("tr34",length*51,0,0);
TGeoTranslation *tr35 = new TGeoTranslation("tr35",length*54,length,0);
TGeoTranslation *tr36 = new TGeoTranslation("tr36",length*57,0,0);
TGeoTranslation *tr37 = new TGeoTranslation("tr37",length*60,length,0);
TGeoTranslation *tr38 = new TGeoTranslation("tr38",length*63,0,0);
TGeoTranslation *tr39 = new TGeoTranslation("tr39",length*66,length,0);
TGeoTranslation *tr40 = new TGeoTranslation("tr40",length*69,0,0);
TGeoTranslation *tr41 = new TGeoTranslation("tr41",length*72,length,0);
TGeoTranslation *tr42 = new TGeoTranslation("tr42",length*75,0,0);
TGeoTranslation *tr43 = new TGeoTranslation("tr43",length*78,length,0);
TGeoTranslation *tr44 = new TGeoTranslation("tr44",length*81,0,0);
TGeoTranslation *tr45 = new TGeoTranslation("tr45",length*84,length,0);
TGeoTranslation *tr46 = new TGeoTranslation("tr46",length*87,0,0);
TGeoTranslation *tr47 = new TGeoTranslation("tr47",length*90,length,0);
TGeoTranslation *tr48 = new TGeoTranslation("tr48",length*93,0,0);

```

```

TGeoTranslation *tr49 = new TGeoTranslation("tr49",length*96,length,0);
TGeoTranslation *tr50 = new TGeoTranslation("tr50",length*99,0,0);
TGeoTranslation *tr51 = new TGeoTranslation("tr51",length*102,length,0);
TGeoTranslation *tr52 = new TGeoTranslation("tr52",length*105,0,0);
TGeoTranslation *tr53 = new TGeoTranslation("tr53",length*108,length,0);
TGeoTranslation *tr54 = new TGeoTranslation("tr54",length*111,0,0);
TGeoTranslation *tr55 = new TGeoTranslation("tr55",length*114,length,0);
TGeoTranslation *tr56 = new TGeoTranslation("tr56",length*117,0,0);
TGeoTranslation *tr57 = new TGeoTranslation("tr57",length*120,length,0);
TGeoTranslation *tr58 = new TGeoTranslation("tr58",length*123,0,0);
TGeoTranslation *tr59 = new TGeoTranslation("tr59",length*126,length,0);
TGeoTranslation *tr60 = new TGeoTranslation("tr60",length*129,0,0);
TGeoTranslation *tr61 = new TGeoTranslation("tr61",length*132,length,0);
TGeoTranslation *tr62 = new TGeoTranslation("tr62",length*135,0,0);
TGeoTranslation *tr63 = new TGeoTranslation("tr63",length*138,length,0);
TGeoTranslation *tr64 = new TGeoTranslation("tr64",length*141,0,0);
TGeoTranslation *tr65 = new TGeoTranslation("tr65",length*144,length,0);
TGeoTranslation *tr66 = new TGeoTranslation("tr66",length*147,0,0);
TGeoTranslation *tr67 = new TGeoTranslation("tr67",length*150,length,0);
TGeoTranslation *tr68 = new TGeoTranslation("tr68",length*153,0,0);
TGeoTranslation *tr69 = new TGeoTranslation("tr69",length*156,length,0);
TGeoTranslation *tr70 = new TGeoTranslation("tr70",length*159,0,0);
TGeoTranslation *tr71 = new TGeoTranslation("tr71",length*162,length,0);
TGeoTranslation *tr72 = new TGeoTranslation("tr72",length*165,0,0);
TGeoTranslation *tr73 = new TGeoTranslation("tr73",length*168,length,0);
TGeoTranslation *tr74 = new TGeoTranslation("tr74",length*171,0,0);
TGeoTranslation *tr75 = new TGeoTranslation("tr75",length*174,length,0);
TGeoTranslation *tr76 = new TGeoTranslation("tr76",length*177,0,0);
TGeoTranslation *tr77 = new TGeoTranslation("tr77",88.5*length,width+width2+length,0);
TGeoTranslation *tr78 = new TGeoTranslation("tr78",88.5*length,-width-width2,0);
TGeoTranslation *tr79 = new TGeoTranslation("tr79",length*186,length,0);

```

```
tr17- >RegisterYourself();
```

tr18– >RegisterYourself();
tr19– >RegisterYourself();
tr20– >RegisterYourself();
tr21– >RegisterYourself();
tr22– >RegisterYourself();
tr23– >RegisterYourself();
tr24– >RegisterYourself();
tr25– >RegisterYourself();
tr26– >RegisterYourself();
tr27– >RegisterYourself();
tr28– >RegisterYourself();
tr29– >RegisterYourself();
tr30– >RegisterYourself();
tr31– >RegisterYourself();
tr32– >RegisterYourself();
tr33– >RegisterYourself();
tr34– >RegisterYourself();
tr35– >RegisterYourself();
tr36– >RegisterYourself();
tr37– >RegisterYourself();
tr38– >RegisterYourself();
tr39– >RegisterYourself();
tr40– >RegisterYourself();
tr41– >RegisterYourself();
tr42– >RegisterYourself();
tr43– >RegisterYourself();
tr44– >RegisterYourself();
tr45– >RegisterYourself();
tr46– >RegisterYourself();
tr47– >RegisterYourself();
tr48– >RegisterYourself();
tr49– >RegisterYourself();
tr50– >RegisterYourself();

```
tr51- >RegisterYourself();
tr52- >RegisterYourself();
tr53- >RegisterYourself();
tr54- >RegisterYourself();
tr55- >RegisterYourself();
tr56- >RegisterYourself();
tr57- >RegisterYourself();
tr58- >RegisterYourself();
tr59- >RegisterYourself();
tr60- >RegisterYourself();
tr61- >RegisterYourself();
tr62- >RegisterYourself();
tr63- >RegisterYourself();
tr64- >RegisterYourself();
tr65- >RegisterYourself();
tr66- >RegisterYourself();
tr67- >RegisterYourself();
tr68- >RegisterYourself();
tr69- >RegisterYourself();
tr70- >RegisterYourself();
tr71- >RegisterYourself();
tr72- >RegisterYourself();
tr73- >RegisterYourself();
tr74- >RegisterYourself();
tr75- >RegisterYourself();
tr76- >RegisterYourself();
tr77- >RegisterYourself();
tr78- >RegisterYourself();
tr79- >RegisterYourself();
```

```
TGeoBBox *box = new TGeoBBox("box",2.,2.,2.);
TGeoBBox *headshape = new TGeoBBox("headshape",1.9,1.9,1.9);
TGeoBBox *det1 = new TGeoBBox("det1", lenght, widht, thick);
```

```
TGeoBBox *det2 = new TGeoBBox("det2", lenght, widht, thick);
TGeoBBox *det3 = new TGeoBBox("det3", lenght, widht, thick);
TGeoBBox *det4 = new TGeoBBox("det4", lenght, widht, thick);
TGeoBBox *det5 = new TGeoBBox("det5", lenght, widht, thick);
TGeoBBox *det6 = new TGeoBBox("det6", lenght, widht, thick);
TGeoBBox *det7 = new TGeoBBox("det7", lenght, widht, thick);
TGeoBBox *det8 = new TGeoBBox("det8", lenght, widht, thick);
TGeoBBox *det9 = new TGeoBBox("det9", lenght, widht, thick);
TGeoBBox *det10 = new TGeoBBox("det10", lenght, widht, thick);
TGeoBBox *det11 = new TGeoBBox("det11", lenght, widht, thick);
TGeoBBox *det12 = new TGeoBBox("det12", lenght, widht, thick);
TGeoBBox *det13 = new TGeoBBox("det13", lenght, widht, thick);
TGeoBBox *det14 = new TGeoBBox("det14", lenght, widht, thick);
TGeoBBox *det15 = new TGeoBBox("det15", lenght, widht, thick);
TGeoBBox *det16 = new TGeoBBox("det16", lenght, widht, thick);
TGeoBBox *det17 = new TGeoBBox("det17", lenght, widht, thick);
TGeoBBox *det18 = new TGeoBBox("det18", lenght, widht, thick);
TGeoBBox *det19 = new TGeoBBox("det19", lenght, widht, thick);
TGeoBBox *det20 = new TGeoBBox("det20", lenght, widht, thick);
TGeoBBox *det21 = new TGeoBBox("det21", lenght, widht, thick);
TGeoBBox *det22 = new TGeoBBox("det22", lenght, widht, thick);
TGeoBBox *det23 = new TGeoBBox("det23", lenght, widht, thick);
TGeoBBox *det24 = new TGeoBBox("det24", lenght, widht, thick);
TGeoBBox *det25 = new TGeoBBox("det25", lenght, widht, thick);
TGeoBBox *det26 = new TGeoBBox("det26", lenght, widht, thick);
TGeoBBox *det27 = new TGeoBBox("det27", lenght, widht, thick);
TGeoBBox *det28 = new TGeoBBox("det28", lenght, widht, thick);
TGeoBBox *det29 = new TGeoBBox("det29", lenght, widht, thick);
TGeoBBox *det30 = new TGeoBBox("det30", lenght, widht, thick);
TGeoBBox *det31 = new TGeoBBox("det31", lenght, widht, thick);
TGeoBBox *det32 = new TGeoBBox("det32", lenght, widht, thick);
TGeoBBox *det33 = new TGeoBBox("det33", lenght, widht, thick);
TGeoBBox *det34 = new TGeoBBox("det34", lenght, widht, thick);
```

```

TGeoBBox *det35 = new TGeoBBox("det35", lenght, widht, thick);
TGeoBBox *det36 = new TGeoBBox("det36", lenght, widht, thick);
TGeoBBox *det37 = new TGeoBBox("det37", lenght, widht, thick);
TGeoBBox *det38 = new TGeoBBox("det38", lenght, widht, thick);
TGeoBBox *det39 = new TGeoBBox("det39", lenght, widht, thick);
TGeoBBox *det40 = new TGeoBBox("det40", lenght, widht, thick);
TGeoBBox *det41 = new TGeoBBox("det41", lenght, widht, thick);
TGeoBBox *det42 = new TGeoBBox("det42", lenght, widht, thick);
TGeoBBox *det43 = new TGeoBBox("det43", lenght, widht, thick);
TGeoBBox *det44 = new TGeoBBox("det44", lenght, widht, thick);
TGeoBBox *det45 = new TGeoBBox("det45", lenght, widht, thick);
TGeoBBox *det46 = new TGeoBBox("det46", lenght, widht, thick);
TGeoBBox *det47 = new TGeoBBox("det47", lenght, widht, thick);
TGeoBBox *det48 = new TGeoBBox("det48", lenght, widht, thick);
TGeoBBox *det49 = new TGeoBBox("det49", lenght, widht, thick);
TGeoBBox *det50 = new TGeoBBox("det50", lenght, widht, thick);
TGeoBBox *det51 = new TGeoBBox("det51", lenght, widht, thick);
TGeoBBox *det52 = new TGeoBBox("det52", lenght, widht, thick);
TGeoBBox *det53 = new TGeoBBox("det53", lenght, widht, thick);
TGeoBBox *det54 = new TGeoBBox("det54", lenght, widht, thick);
TGeoBBox *det55 = new TGeoBBox("det55", lenght, widht, thick);
TGeoBBox *det56 = new TGeoBBox("det56", lenght, widht, thick);
TGeoBBox *det57 = new TGeoBBox("det57", lenght, widht, thick);
TGeoBBox *det58 = new TGeoBBox("det58", lenght, widht, thick);
TGeoBBox *det59 = new TGeoBBox("det59", lenght, widht, thick);
TGeoBBox *det60 = new TGeoBBox("det60", lenght, widht, thick);
TGeoBBox *det61 = new TGeoBBox("det61", lenght*89.5, widht2, thick);
TGeoBBox *det62 = new TGeoBBox("det62", lenght*89.5, widht2, thick);

```

```

TGeoVolume *world = new TGeoVolume("world",box,Vacuum);

```

```

geom->SetTopVolume(world);

```

```
TGeoVolume *head = new TGeoVolume("head",headshape,Vacuum);
TGeoVolume *detector1 = new TGeoVolume("detector1",det1, Diamond);
TGeoVolume *detector2 = new TGeoVolume("detector2",det2, Diamond);
TGeoVolume *detector3 = new TGeoVolume("detector3",det3, Diamond);
TGeoVolume *detector4 = new TGeoVolume("detector4",det4, Diamond);
TGeoVolume *detector5 = new TGeoVolume("detector5",det5, Diamond);
TGeoVolume *detector6 = new TGeoVolume("detector6",det6, Diamond);
TGeoVolume *detector7 = new TGeoVolume("detector7",det7, Diamond);
TGeoVolume *detector8 = new TGeoVolume("detector8",det8, Diamond);
TGeoVolume *detector9 = new TGeoVolume("detector9",det9, Diamond);
TGeoVolume *detector10 = new TGeoVolume("detector10",det10, Diamond);
TGeoVolume *detector11 = new TGeoVolume("detector11",det11, Diamond);
TGeoVolume *detector12 = new TGeoVolume("detector12",det12, Diamond);
TGeoVolume *detector13 = new TGeoVolume("detector13",det13, Diamond);
TGeoVolume *detector14 = new TGeoVolume("detector14",det14, Diamond);
TGeoVolume *detector15 = new TGeoVolume("detector15",det15, Diamond);
TGeoVolume *detector16 = new TGeoVolume("detector16",det16, Diamond);
TGeoVolume *detector17 = new TGeoVolume("detector17",det17, Diamond);
TGeoVolume *detector18 = new TGeoVolume("detector18",det18, Diamond);
TGeoVolume *detector19 = new TGeoVolume("detector19",det19, Diamond);
TGeoVolume *detector20 = new TGeoVolume("detector20",det20, Diamond);
TGeoVolume *detector21 = new TGeoVolume("detector21",det21, Diamond);
TGeoVolume *detector22 = new TGeoVolume("detector22",det22, Diamond);
TGeoVolume *detector23 = new TGeoVolume("detector23",det23, Diamond);
TGeoVolume *detector24 = new TGeoVolume("detector24",det24, Diamond);
TGeoVolume *detector25 = new TGeoVolume("detector25",det25, Diamond);
TGeoVolume *detector26 = new TGeoVolume("detector26",det26, Diamond);
TGeoVolume *detector27 = new TGeoVolume("detector27",det27, Diamond);
TGeoVolume *detector28 = new TGeoVolume("detector28",det28, Diamond);
TGeoVolume *detector29 = new TGeoVolume("detector29",det29, Diamond);
TGeoVolume *detector30 = new TGeoVolume("detector30",det30, Diamond);
TGeoVolume *detector31 = new TGeoVolume("detector31",det31, Diamond);
TGeoVolume *detector32 = new TGeoVolume("detector32",det32, Diamond);
```

```
TGeoVolume *detector33 = new TGeoVolume("detector33",det33, Diamond);
TGeoVolume *detector34 = new TGeoVolume("detector34",det34, Diamond);
TGeoVolume *detector35 = new TGeoVolume("detector35",det35, Diamond);
TGeoVolume *detector36 = new TGeoVolume("detector36",det36, Diamond);
TGeoVolume *detector37 = new TGeoVolume("detector37",det37, Diamond);
TGeoVolume *detector38 = new TGeoVolume("detector38",det38, Diamond);
TGeoVolume *detector39 = new TGeoVolume("detector39",det39, Diamond);
TGeoVolume *detector40 = new TGeoVolume("detector40",det40, Diamond);
TGeoVolume *detector41 = new TGeoVolume("detector41",det41, Diamond);
TGeoVolume *detector42 = new TGeoVolume("detector42",det42, Diamond);
TGeoVolume *detector43 = new TGeoVolume("detector43",det43, Diamond);
TGeoVolume *detector44 = new TGeoVolume("detector44",det44, Diamond);
TGeoVolume *detector45 = new TGeoVolume("detector45",det45, Diamond);
TGeoVolume *detector46 = new TGeoVolume("detector46",det46, Diamond);
TGeoVolume *detector47 = new TGeoVolume("detector47",det47, Diamond);
TGeoVolume *detector48 = new TGeoVolume("detector48",det48, Diamond);
TGeoVolume *detector49 = new TGeoVolume("detector49",det49, Diamond);
TGeoVolume *detector50 = new TGeoVolume("detector50",det50, Diamond);
TGeoVolume *detector51 = new TGeoVolume("detector51",det51, Diamond);
TGeoVolume *detector52 = new TGeoVolume("detector52",det52, Diamond);
TGeoVolume *detector53 = new TGeoVolume("detector53",det53, Diamond);
TGeoVolume *detector54 = new TGeoVolume("detector54",det54, Diamond);
TGeoVolume *detector55 = new TGeoVolume("detector55",det55, Diamond);
TGeoVolume *detector56 = new TGeoVolume("detector56",det56, Diamond);
TGeoVolume *detector57 = new TGeoVolume("detector57",det57, Diamond);
TGeoVolume *detector58 = new TGeoVolume("detector58",det58, Diamond);
TGeoVolume *detector59 = new TGeoVolume("detector59",det59, Diamond);
TGeoVolume *detector60 = new TGeoVolume("detector60",det60, Diamond);
TGeoVolume *detector61 = new TGeoVolume("detector61",det61, Diamond);
TGeoVolume *detector62 = new TGeoVolume("detector62",det62, Diamond);
```

```
head->AddNode(detector1,1, tr17);
```

```
head->AddNode(detector2,2, tr18);
```



```
head->AddNode(detector3,3, tr19);
head->AddNode(detector4,4, tr20);
head->AddNode(detector5,5, tr21);
head->AddNode(detector6,6, tr22);
head->AddNode(detector7,7, tr23);
head->AddNode(detector8,8, tr24);
head->AddNode(detector9,9, tr25);
head->AddNode(detector10,10, tr26);
head->AddNode(detector11,11, tr27);
head->AddNode(detector12,12, tr28);
head->AddNode(detector13,13, tr29);
head->AddNode(detector14,14, tr30);
head->AddNode(detector15,15, tr31);
head->AddNode(detector16,16, tr32);
head->AddNode(detector17,17, tr33);
head->AddNode(detector18,18, tr34);
head->AddNode(detector19,19, tr35);
head->AddNode(detector20,20, tr36);
head->AddNode(detector21,21, tr37);
head->AddNode(detector22,22, tr38);
head->AddNode(detector23,23, tr39);
head->AddNode(detector24,24, tr40);
head->AddNode(detector25,25, tr41);
head->AddNode(detector26,26, tr42);
head->AddNode(detector27,27, tr43);
head->AddNode(detector28,28, tr44);
head->AddNode(detector29,29, tr45);
head->AddNode(detector30,30, tr46);
head->AddNode(detector31,31, tr47);
head->AddNode(detector32,32, tr48);
head->AddNode(detector33,33, tr49);
head->AddNode(detector34,34, tr50);
head->AddNode(detector35,35, tr51);
```

```
head- >AddNode(detector36,36, tr52);
head- >AddNode(detector37,37, tr53);
head- >AddNode(detector38,38, tr54);
head- >AddNode(detector39,39, tr55);
head- >AddNode(detector40,40, tr56);
head- >AddNode(detector41,41, tr57);
head- >AddNode(detector42,42, tr58);
head- >AddNode(detector43,43, tr59);
head- >AddNode(detector44,44, tr60);
head- >AddNode(detector45,45, tr61);
head- >AddNode(detector46,46, tr62);
head- >AddNode(detector47,47, tr63);
head- >AddNode(detector48,48, tr64);
head- >AddNode(detector49,49, tr65);
head- >AddNode(detector50,50, tr66);
head- >AddNode(detector51,51, tr67);
head- >AddNode(detector52,52, tr68);
head- >AddNode(detector53,53, tr69);
head- >AddNode(detector54,54, tr70);
head- >AddNode(detector55,55, tr71);
head- >AddNode(detector56,56, tr72);
head- >AddNode(detector57,57, tr73);
head- >AddNode(detector58,58, tr74);
head- >AddNode(detector59,59, tr75);
head- >AddNode(detector60,60, tr76);
head- >AddNode(detector61,61, tr77);
head- >AddNode(detector62,62, tr78);

world- >AddNode(head,1,&rot1);

head- >SetVisibility(kFALSE);
detector1- >SetLineColor(kGreen);
detector2- >SetLineColor(kGreen);
```

detector3– >SetLineColor(kGreen);
detector4– >SetLineColor(kGreen);
detector5– >SetLineColor(kGreen);
detector6– >SetLineColor(kGreen);
detector7– >SetLineColor(kGreen);
detector8– >SetLineColor(kGreen);
detector9– >SetLineColor(kGreen);
detector10– >SetLineColor(kGreen);
detector11– >SetLineColor(kGreen);
detector12– >SetLineColor(kGreen);
detector13– >SetLineColor(kGreen);
detector14– >SetLineColor(kGreen);
detector15– >SetLineColor(kGreen);
detector16– >SetLineColor(kGreen);
detector17– >SetLineColor(kGreen);
detector18– >SetLineColor(kGreen);
detector19– >SetLineColor(kGreen);
detector20– >SetLineColor(kGreen);
detector21– >SetLineColor(kGreen);
detector22– >SetLineColor(kGreen);
detector23– >SetLineColor(kGreen);
detector24– >SetLineColor(kGreen);
detector25– >SetLineColor(kGreen);
detector26– >SetLineColor(kGreen);
detector27– >SetLineColor(kGreen);
detector28– >SetLineColor(kGreen);
detector29– >SetLineColor(kGreen);
detector30– >SetLineColor(kGreen);
detector31– >SetLineColor(kGreen);
detector32– >SetLineColor(kGreen);
detector33– >SetLineColor(kGreen);
detector34– >SetLineColor(kGreen);
detector35– >SetLineColor(kGreen);

```
detector36– >SetLineColor(kGreen);
detector37– >SetLineColor(kGreen);
detector38– >SetLineColor(kGreen);
detector39– >SetLineColor(kGreen);
detector40– >SetLineColor(kGreen);
detector41– >SetLineColor(kGreen);
detector42– >SetLineColor(kGreen);
detector43– >SetLineColor(kGreen);
detector44– >SetLineColor(kGreen);
detector45– >SetLineColor(kGreen);
detector46– >SetLineColor(kGreen);
detector47– >SetLineColor(kGreen);
detector48– >SetLineColor(kGreen);
detector49– >SetLineColor(kGreen);
detector50– >SetLineColor(kGreen);
detector51– >SetLineColor(kGreen);
detector52– >SetLineColor(kGreen);
detector53– >SetLineColor(kGreen);
detector54– >SetLineColor(kGreen);
detector55– >SetLineColor(kGreen);
detector56– >SetLineColor(kGreen);
detector57– >SetLineColor(kGreen);
detector58– >SetLineColor(kGreen);
detector59– >SetLineColor(kGreen);
detector60– >SetLineColor(kGreen);
detector61– >SetLineColor(kGreen);
detector62– >SetLineColor(kGreen);
```

```
geom– >CloseGeometry();
geom– >Export("Detector.gdml");
world– >Draw("ogl");
```

Appendix B Source .g4mac file

```
/gras/geometry/type gdml
/gdml/file Detector.gdml
/gdml/setup world

    /gras/physics/addPhysics em_standard_opt3
/gras/physics/addPhysics QBBC
/gras/physics/addPhysics QGSP_BERT_HP
/gras/physics/addPhysics raddecay
/gras/physics/addPhysics bertini_hp
/gras/physics/addPhysics elasticHP
/gras/physics/addPhysics gamma_nuc
/gras/physics/addPhysics stopping
/gras/physics/addPhysics secondary_generator

/run/initialize

    /gps/particle neutron
/gps/pos/type Point
/gps/pos/centre 0.174 0 0.01 cm
/gps/direction 0 0 -1
/gps/ene/type Mono
/gps/energy 14 MeV

    /vis/scene/create
/vis/open VRML2FILE
/vis/scene/endOfEventAction accumulate 10000
/tracking/storeTrajectory 1
/vis/scene/endOfEventAction accumulate
/gras/event/drawEvents all
/gras/event/drawTracks all
```

```
/gras/analysis/dose/addModule EdepInDiode1  
/gras/analysis/dose/EdepInDiode1/addVolume detector30_PV  
/gras/analysis/dose/EdepInDiode1/setUnit MeV
```

```
/gras/analysis/setNormalisationType NONORMALIZATION
```

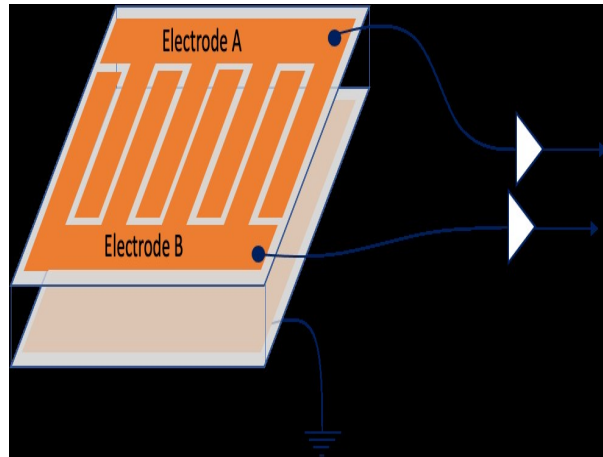
```
/gras/analysis/CSVOutput 0  
/gras/event/printModulo 50000
```

```
/gras/histo/fileName kk  
/run/beamOn 1000000
```

7 Prošireni sažetak

7.1 Uvod

Poluvodički detektori su detektori bazirani na poluvodičkim materijalima (siliciju ili dijamantu najčešće) i njihovim svojstvima. Njihov razvoj započinje pedesetih godina prošlog stoljeća dok komercijalna upotreba počinje sedamdesetih godina. Koriste se za detekciju električno nabijenih čestica kao što su protoni, alfa čestice i ostali ioni s obzirom da nabijene čestice pri prolasku kroz materiju uzrokuju elektromagnetske procese koji mogu biti promatrani i izmjereni. Poluvodički detektori mogu biti korišteni i za detekciju neutralnih čestica kao što su neutroni ili za detekciju gama zračenja. Detekcija gama zračenja i neutronske zračenja ne odvija se direktno nego detekcijom sekundarnih čestica koje nastaju interakcijom neutralnih čestica s materijom. Neutroni u nuklearnim reakcijama uzrokuju nastanak alfa čestica koje potom mogu biti detektirane, dok se gama zračenje detektira preko Comptonovih elektrona koji nastaju interakcijom gama zračenja i materije. Dijamantni detektori su odlični poluvodički detektori zbog svojstava kao što su mala struja curenja, kapacitet, visoka osjetljivost, visoka otpornost na zračenje i otpornost na visoke temperature. S obzirom na takva svojstva mogu imati široku primjenu i to u područjima sa teškim uvjetima primjerice na visokim temperaturama npr. u fuzijskim reaktorima. Glavna ideja ovog rada je dizajniranje i testiranje nove konfiguracije dijamantnog detektora dizajnirane u Laboratoriju za interakcije ionskih snopova na Institutu Ruđer Bošković u Zagrebu za diskriminaciju neutronske i gama zračenja koja može biti primijenjena ne samo na sobnoj temperaturi nego i na jako niskim i visokim temperaturama uz jako pozadinsko zračenje. Kod takve geometrije, alfa čestica nastala interakcijom neutronske s materijalom inducira signal u jednoj elektrodi detektora, dok Comptonov elektron nastao interakcijom materije i gama zračenja inducira signal u obje elektrode. Ovakav detektor, dizajniran je na temelju patenta dr. sc. Milka Jakšića, dr. sc. Georgiosa Provatasa i dr. sc. Andrea Crnjca prikazana koji je prikazan na Slici 7.1.

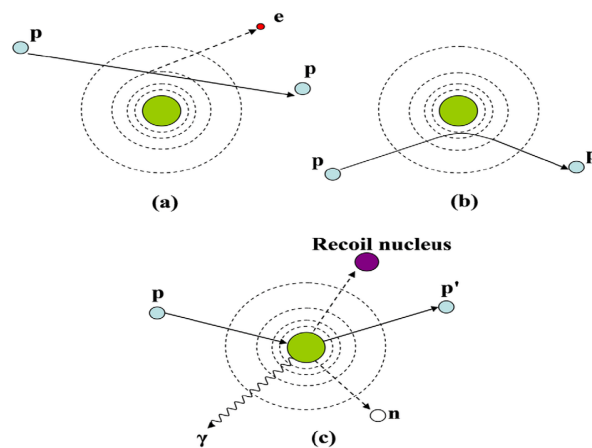


Slika 7.1: Predloženi dizajn CVD dijamantnog detektora za diskriminaciju brzih neutrona od gama zračenja od strane dr. sc. Milka Jakšića, dr. sc. Georgiosa Provatasa i dr. sc. Andrea Crnjca.

7.2 Teorijska pozadina

7.2.1 Interakcije čestica i materije

Kada je riječ o interakcijama čestica i materije bit će promatrani protoni, neutroni i gama zrake. Kada nabijena čestica prolazi kroz materiju odvijaju se dva glavna procesa, gubitak energije čestice te otklon čestice od upadnog smjera uzrokovan elastičnim raspršenjem. Ovi procesi uzrokovani su neelastičnim sudarima sa slobodnim i atomskim elektronima, atomima metama i elastičnim raspršenjem. Ostali procesi koji se mogu odviti su Čerenkovljevo zračenje, zakočno zračenje te nuklearne reakcije. Gubitak energije nabijene čestice pri prolasku kroz materijal opisan je zaustavnom snagom koja je definirana kao dE/dx i može biti elektronička, nuklearna ili radijativna. Interakcija protona s materijom odvija se kroz tri glavna procesa prikazana na Slici 7.2, (a) neelastična Coulombova interakcija sa atomskim elektronima koja čini najzastupljeniji proces, (b) Coulombovo raspršenje sa atomskim jezgama i (c) neelastične nuklearne reakcije. Interakcije neutrona s materijom odvijaju se također kroz više procesa, ali oni ne uključuju Coulombovu interakciju s obzirom da neutroni nisu električno nabijene čestice. Glavna interakcija neutrona sa materijom je preko kratkodosežne jake sile sa jezgama. Takvi procesi uključuju elastično raspršenje, neelastično raspršenje, radijativni uhvat neutrona, nuklearne reakcije u kojima je neutron uhvaćen i emitirane su nabijene čestice te fisiju i proizvodnju hadronskih pljusкова. Koji od ovih procesa će se odviti ovisi o energiji neutrona.



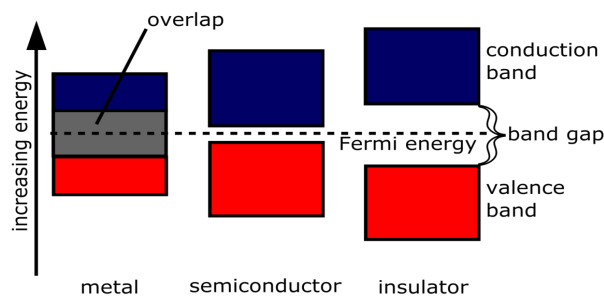
Slika 7.2: Ilustrirana interakcija protona i materije: (a) neelastična Coulomb interakcija, (b) elastično Coulombovo raspršenje, (c) nuklearne reakcije.[10]

Naposljetku, interakcija gama zračenja sa materijom odvija se preko fotoelektričnog efekta, Comptonovog raspršenja i proizvodnje para.

7.2.2 Poluvodički i dijamantni detektori

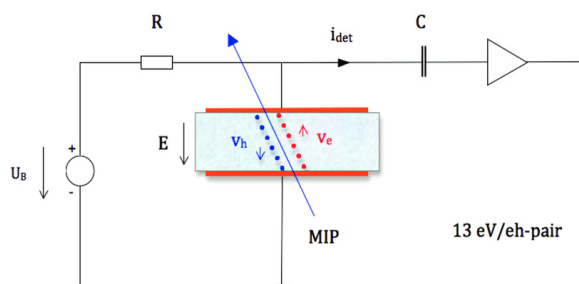
Ionizirajuće zračenje detektira se na principu konverzije energije čestice u nositelje naboja u osjetljivom volumenu detektora. Naboj se prikuplja primjenom električnog polja i potom pretvara u puls ili signal korištenjem pretpojačala i pojačala. Glavna svojstva detektora su osjetljivost na zračenje, energetska rezolucija, Fano-faktor, funkcija odgovora i vrijeme odgovora, učinkovitost i "mrtvo" vrijeme. Poluvodički detektori baziraju se na poluvodičkim materijalima koji se od vodiča i izolatora razlikuju u strukturi energetske vrpce. Kod izolatora postoji procjep između valentne i vodljive vrpce koji onemogućuje prelazak elektrona iz jedne vrpce u drugu, dok kod vodiča postoji preklop između vrpca i elektroni mogu prelaziti iz jedne vrpce u drugu slobodno što omogućava vođenje struje. Poluvodiči, kao i izolatori imaju procjep između vrpca, međutim on je manji nego u izolatora te u povoljnim uvjetima elektroni mogu preći iz jedne vrpce u drugu. Struktura energetske vrpce izolatora, vodiča i poluvodiča prikazana je na Slici 7.3.

Dvije važne vrste poluvodičkih detektora su dijamantni detektori bazirani na dijamantima i detektori sa površinskom barijerom bazirani na siliciju i Schottky barijerama. Schottky barijere nastaju na spoju poluvodiča i metala koji imaju različite Fermijeve nivoe. Dijamantni detektori imaju energiju potrebnu za proizvodnju para elektron-šupljina od 13 eV/paru [2]. Na Slici 7.4 njihov način rada je prikazan;



Slika 7.3: Energetska vrpca vodiča, poluvodiča i izolatora.[11]

ulazna čestica ionizira elektrone i šupljine koje struje prema elektrodama zbog električnog polja uzrokovano naponom na detektoru. Spajanjem na pojačalo osjetljivo na naboj inducira se naponski signal proporcionalan sakupljenom naboju. Usporedba



Slika 7.4: Način rada dijamantnih detektora. [4]

svojstava dijamanta u odnosu na silicij prikazana je u Tablici 7.1. Iz Tablice 7.1

Svojstvo	Silicij	Dijamant
Energetski procjep (eV)	1.12	5.5
Probojno polje (V/mm)	$3 \cdot 10^5$	10^7
Gustoća intrinzičnih nosilaca naboja (cm^{-3})	$1.5 \cdot 10^{10}$	$< 10^3$
Masena gustoća (g/cm^3)	2.33	3.52
Dielektrična konstanta	11.9	5.7
Energija pomaka (eV/atom)	13-20	43
Energija za stvaranje para (eV)	3.6	13
Otpornost (Ω)	$2.23 \cdot 10^5$	$> 10^{12}$
Mobilnost šupljina (cm^2Vs^{-1})	480	2100
Mobilnost elektrona (cm^2Vs^{-1})	13350	2400

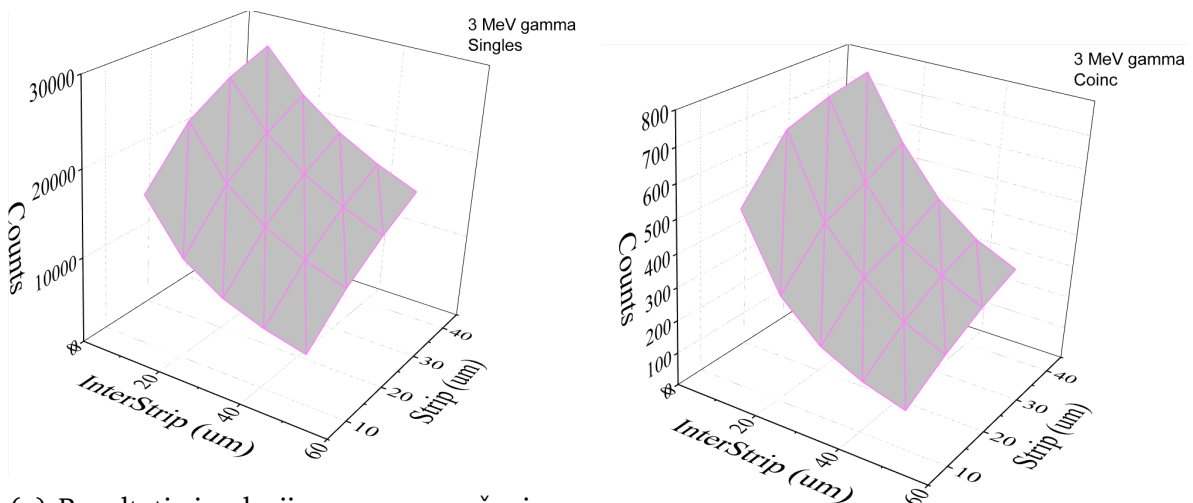
Tablica 7.1: Usporedba svojstava dijamanta i silicija.[1]

je vidljivo da dijamant ima veći energetski procjep i potrebna je veća energija za stvaranje elektron-šupljina para. Uz to dijamant ima veću otpornost i veće polje proboja kao i veću mobilnost šupljina od silicija, te manju dielektričnu konstantu i

mobilnost elektrona. Važno je napomenuti da je dijamant i fizički čvršći te je testiran u područjima visokih i niskih temperatura od približno 100 K do oko 1000 K [27, 28].

7.3 Simulacije

Monte-Carlo simulacije su izvedene pomoću ESA softvera GRAS baziranog na Geant4 [19], te CERN-ovog znanstvenog alata ROOT¹⁰[20]. Koristeći ove alate definirana je i vizualizirana geometrija detektora, izvor zračenja te izvedena analiza. Koristeći simulacije za gama zračenje energije 3 MeV-a i neutronske zračenje energije 14.5 MeV-a definirana je potrebna geometrija za izradu detektora tako što je odabrana širina trake detektora kao ona širina na kojoj je najveća simulirana detekcija neutrona, a najmanja detekcija gama zračenja (što je širina trake od 40 μm , a širina između traka 20 μm). Ova geometrija, međutim nije odabrana zbog ograničenja opreme za pripremu detektora, te je na posljetku odabrana širina trake i međuprostora od 30 μm . Rezultati simulacija za gama zračenje i neutrone prikazani su na Slici 7.5 a i b i 7.6 a i b. Simulacije koje su nadalje korištene su one SRIM Programskog paketa¹¹



(a) Rezultati simulacija za gama zračenje energije 3 MeV-a u slučaju pojedinačnih događaja.

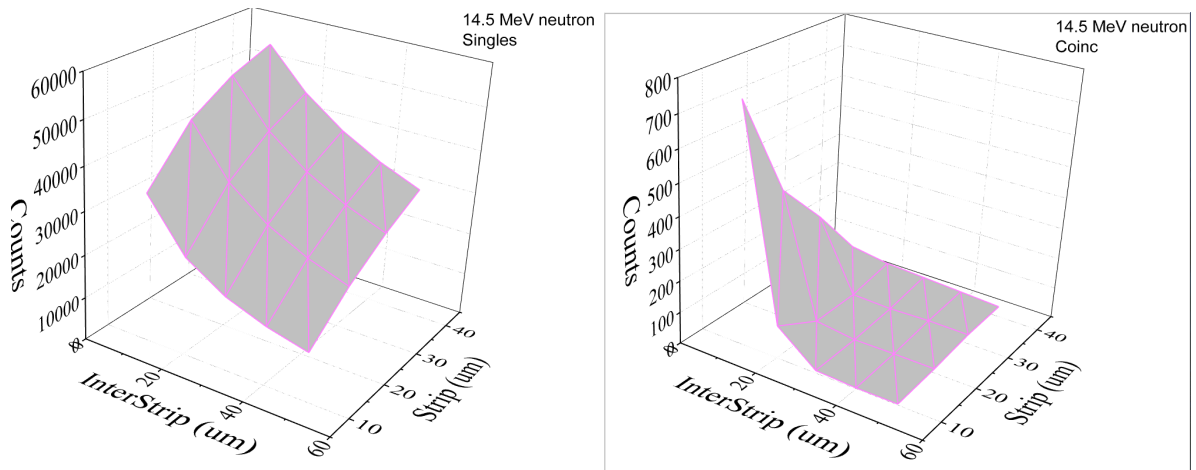
(b) Rezultati simulacija za gama zračenje energije 3 MeV-a u slučaju koincidencija.

Slika 7.5: Rezultati simulacija za gama zračenje.

autora James F. Zieglera koje omogućavaju vizualizaciju ionizacijskih profila za različite ione, medije i energije, distribucije iona u medijima te simulaciju raspona zaustavljanja i zaustavne snage.

¹⁰<https://root.cern/>

¹¹<http://www.srim.org/>



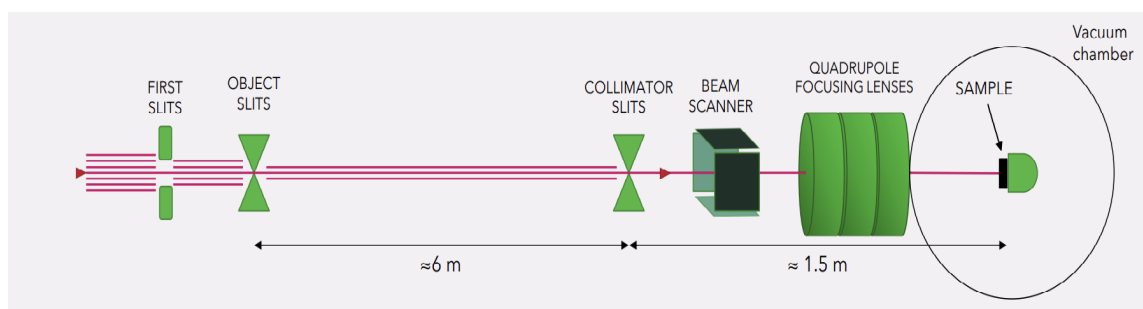
(a) Rezultati simulacija za neutronske zračenje energije 14.5 MeV u pojedinačnom slučaju.
 (b) Rezultati simulacija za neutronske zračenje energije 14.5 MeV u slučaju koincidencija.

Slika 7.6: Rezultati simulacija za neutronske zračenje.

7.4 Eksperimentalne metode i postav

Mjerenja su izvedena u Laboratoriju za interakcije ionskih snopova Instituta Ruđer Bošković, te akceleratori korišteni pri mjerenjima su 6.0 MV Tandem Van de Graaf te 1.0 MV Tandetron akcelerator.

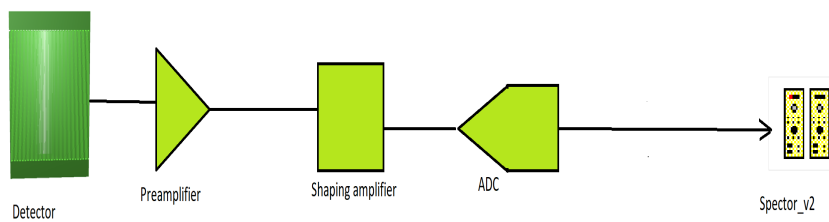
Ilustracija eksperimentalne linije prikazana je nadalje na Slici 7.8, dok je elektronički postav korišten shematski prikazan na Slici 7.9. Pojača korištena u mjerenjima su Ortec 570, Canberra 2022 i Ortec 572 dok su ADC-ovi korišteni Canberra Fast ADC 8075 i 8077 u mjerenjima pojedinačnih događaja. U mjerenjima koincidencija



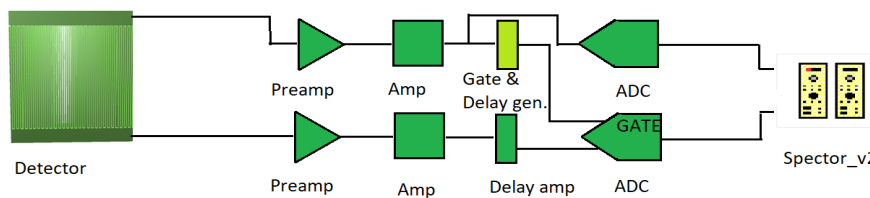
Slika 7.7: Ilustracija eksperimentalne linije. Izradio dr. sc. Andreo Crnjac.

korišteno je još i pojačalo kašnjenja (Ortec Model 427 A) te generator kašnjenja i ulaza (Ortec Model 416 A Gate & Delay Generator). Uz to korištena su i tri pojačala Canberra Spectroscopy Amplifier Model 2020, Canberra Amplifier 2026 i Ortec 672 Spectroscopy Amplifier, dok su analogno-digitalni pretvarači (ADC - engl. *Analog to*

Digital Coverter) korišteni bili Canberra ADC 8075. Elektronički lanac za mjerenje koincidencija prikazan je na Slici 7.10.



Slika 7.8: Elektronički lanac za prikupljanje podataka u pojedinačnom načinu rada.

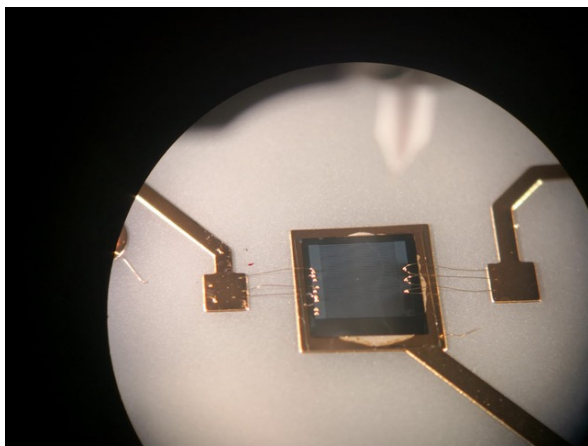


Slika 7.9: Elektronički lanac za prikupljanje podataka u mjerenju koincidencija.

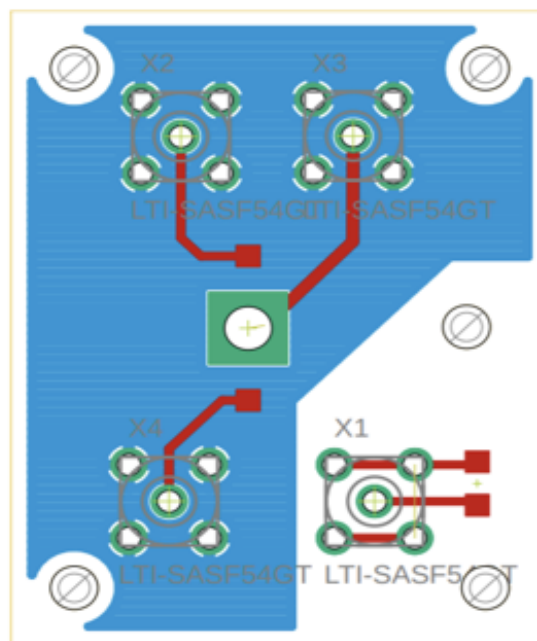
Eksperimentalne linije korištene su E3 dualna mikroproba, te E9 ionska mikroproba, a metode korištene su STIM - Skenirajuća transmisijska ionska mikroskopija, tehnika kojom se detektiraju transmitirani ioni, i način na koji čestice gube energiju u uzorku daje informaciju o gustoći i strukturi uzorka, te IBIC (engl. *Ion Beam Induced Charge*). IBIC metoda se bazira na prikupljanju naboja induciranog prolaskom ionskog snopa kroz uzorak ili detektor. Dijamantni kristal (scCVD) je kupljen od kompanije Element Six¹², površine je 4x4 i debljine 40 μm . Dijamantni kristal prikazan je na Slici 7.10 (a) nakon što je uzorak elektroda nanesen u CEA LIST Laboratoriju za dijamantne senzore te je napravljeno spajanje zlatnom žicom kako bi se postigli kontakti. Širina jedne pruge je 30 μm . Matična ploča je dizajnirana u Laboratoriju za interakcije ionskih snopova te je prikazana na Slici 7.10 (b), a izradila ju je kom-

¹²<https://www.e6.com/>

panija PCBONLINE¹³. Mjerenja su vršena sa protonskim snopovima energija 2, 1.8 i



(a) Uzorak nakon što je uzorak elektroda nanesen.



(b) Dizajn PCB ploče.

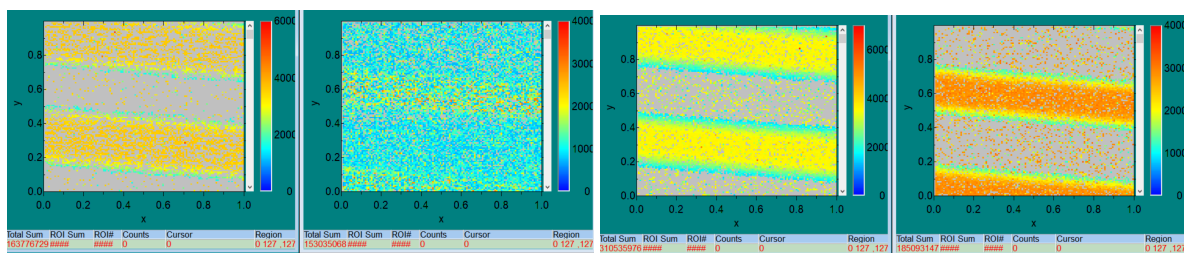
Slika 7.10: Izrada detektora i dizajn matične ploče.

3.5 MeV-a.

7.5 Rezultati

Prvo mjerenje napravljeno je ono sa protonskim snopom energije 2 MeV-a. Nakon što je izračunata stvarna veličina piksela koristeći set bakrenih mrežica promatrane su IBIC mape elektroda. Na Slici 7.11 prikazane su IBIC mape elektroda na pozitivnim naponima snimljene koristeći ovu energiju snopa, vidljivo je da na (a) dijelu slike gdje su obje elektrode na istom naponu od 5 V one nisu simetrične s obzirom da je struja curenja na jednoj $0.02 \mu A$. Na (b) dijelu Slike 7.11 gdje je jedne elektrode, ona bez šuma stavljena sada na napon 3 V kako bi se kompenzirao šum sa druge elektrode, vidljivo je da su sada snimljene IBIC mape elektroda simetrične. Sljedeće mjerenje napravljeno jeste mjerenje sa protonskim snopom energije 3.5 MeV-a, ovdje je bitno napomenuti da snop energije 2 MeV-a deponira svu svoju energiju u detektoru, dok snop energije 3.5 MeV-a prolazi kroz detektor i deponira samo dio svoje energije u osjetljivom volumenu detektora. IBIC mape elektroda snimljene sa protonskim snopom ove energije prikazane su na Slici 7.12 i to sa elektrodama na negativnim

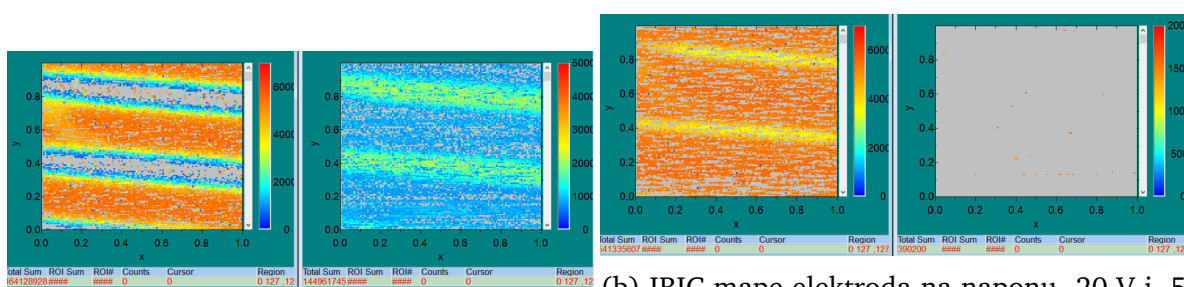
¹³<https://www.pcbonline.com/>



(a) IBIC mape elektroda s primjenjenim naponom 5 V na obje elektrode. (b) IBIC mape elektroda s primjenjenim naponom 5 V i 3 V.

Slika 7.11: IBIC mape obje gornje elektrode detektora na pozitivnim naponima uz energiju protonskog snopa 2MeV-a.

naponima. CCE (engl. *Charge Collection efficiency*) ili efikasnost prikupljanja naboja



(a) IBIC mape elektroda na naponu -5 V. (b) IBIC mape elektroda na naponu -20 V i -5 V.

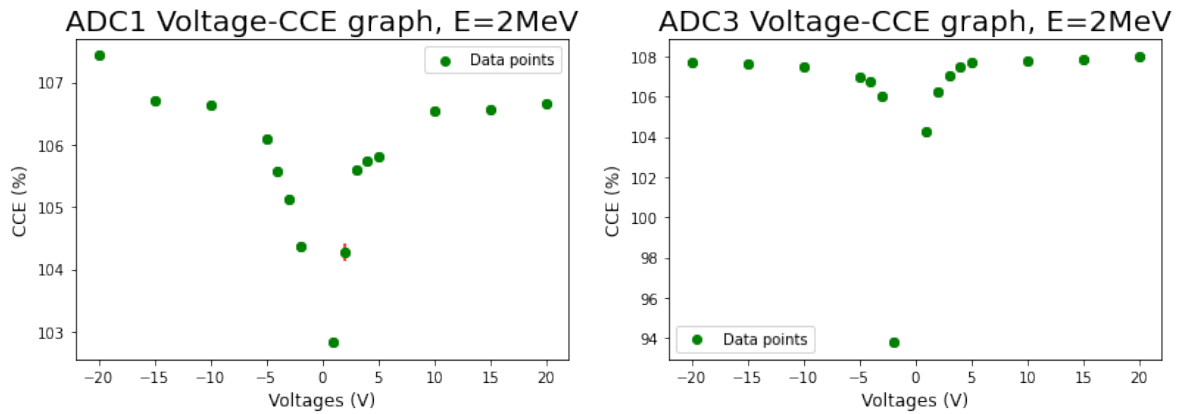
Slika 7.12: IBIC mape elektroda na negativnim naponima uz energiju protonskog snopa 3.5 MeV-a.

računa se sljedećom formulom:

$$CCE_{Diamond} = 100\% \cdot \frac{A_{Diamond} G_{Si} B_{Si}}{A_{Si} G_{Diamond} B_{Diamond}} \quad (7.1)$$

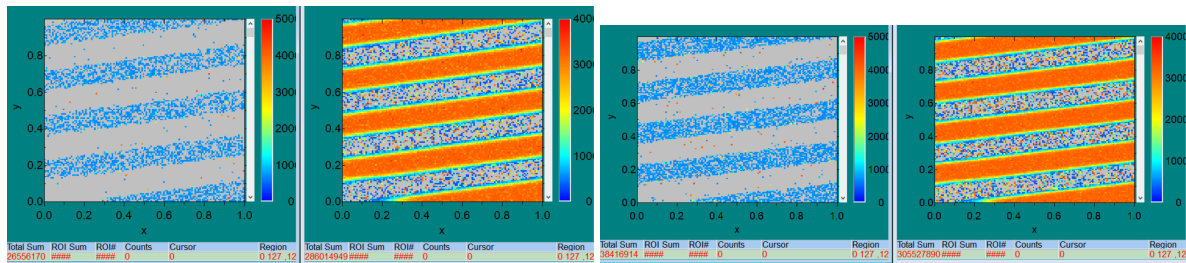
Ovdje je A kanal u kojem se pojavljuje maksimum spektra snimljenog za silicij ili dijamant, G je uvećanje korišteno, dok je B broj parova elektron-šupljina stvorenih na zadanoj energiji za dijamant ili silicij. Silicijski detektor (STIM) koji je SSB detektor ima CCE 100% te se taj podatak koristi u računanju CCE-a za dijamant. Krivulja CCE-Napon ovisnosti prikazana je na Slici 7.13. a i b, uz energiju protonskog snopa 2 MeV.

Snimljene mape za mjerenja koincidencija prikazane su na Slici 7.14. uz energiju snopa 1.8 MeV-a.



(a) CCE-Napon graf za jednu gornju elektrodu spojenu na ADC1 uz energiju protonskog snopa 2 MeV-a. (b) CCE-Napon graf za drugu gornju elektrodu spojenu na ADC3 uz energiju protonskog snopa 2 MeV-a.

Slika 7.13: CCE-Napon graf za gornje elektrode detektora.



Slika 7.14: IBIC mape za mjerenja koincidencija na različitim naponima.

7.6 Zaključak

U ovom radu izrađen je i testiran novi dijamantni detektor za razlikovanje brzih neutrona od gama zračenja. Ovakav detektor dizajniran je s ciljem korištenja u težim uvjetima jakog pozadinskog zračenja i visokih temperatura. U takvim uvjetima dijamant je najbolji materijal za rad s obzirom na otpornost na visoke temperature, dok je upravo ovakva geometrija korisna s obzirom da će alfa čestice kao sekundarne čestice nastale interakcijom neutrona i materije izazvati signal u samo jednoj elektrodi dok će elektroni nastali kao produkt interakcije gama zračenja i materije izazvati odgovor u obje elektrode detektora. U izvedenim mjerenjima pojedinačnih događaja (engl. *single mode*) testirano je da je CCE ovakvog detektora 100% te su bilo kakve fluktuacije uzrokovane nelinearnošću odgovora u elektroničkom lancu. Mjerenjima sa koincidencijama (engl. *coincidence mode*) dokazano je da elektrode detektora funkcioniraju kao zasebni detektori. Sljedeći korak u radu sa ovakvim de-

tektorom bio bi izlaganje direktnom neutronsom i gama zračenju te potom mjerenje i na visokim i niskim temperaturama.

Bibliography

- [1] Koizumi, S.; Nebel, C.; Nesladek, M. Physics and Applications of CVD Diamond, Weinheim; WILEY-VCH Verlag GmbH & Co. KGaA, 2008.
- [2] Pan, L.S.; Kania, D. R. Diamond: Electronic Properties and Applications, Boston; Dordrecht; London : Kluwer academic publ., 1995.
- [3] Leo, W. R. Techniques for Nuclear and Particle Physics Experiments A How-to Approach, Berlin; Heidelberg, New York: Springer-Verlag, 1987.
- [4] Griesmayer, E.; Dehning, Bernd. Diamonds for Beam Instrumentation. // Physics Procedia. 37. 1997-2004. 10.1016/j.phpro.2012.02.526 (2012).
- [5] Manninen, A.L. CLINICAL APPLICATIONS OF RADIOPHOTOLUMINESCENCE (RPL) DOSIMETRY IN EVALUATION OF PATIENT RADIATION EXPOSURE IN RADIOLOGY Determination of absorbed and effective dose (2014).
- [6] Cosic, D., Provatas, G., Vicentijevic M., Rodrigez Ramos M., Crnjac A., Jaksic M., Tadic T., Begusic, D., (2020). Fast pulse processing concept for uLoss Monitors at IFMIF-DONES. 31st Symposium on Fusion Technology (SOFT2020)
- [7] Ruder Boskovic Institute, Laboratory for ion beam interactions <https://www.irb.hr/Zavodi/Zavod-za-eksperimentalnu-fiziku/Laboratorij-za-interakcije-ionskih-snopova>, 21.08.2022.
- [8] Scrivens, Richard and Kronberger, Matthias and Kuchler, Detlef and Lettry, J. and Mastrostefano, C. and Midttun, Øystein and O'Neil, M. and Pereira, H. and Schmitzer, Claus. Overview of the status and developments on primary ion sources at CERN. (2022).
- [9] National Electrostatics Corp. Source of Negative Ions by Cesium Sputtering (SNICS) <https://www.pelletron.com/products/snics/>, 21.08.2022.
- [10] Newhauser, Wayne; Zhang, Rui. The physics of proton therapy. Physics in medicine and biology. 60. R155-R209. 10.1088/0031-9155/60/8/R155. (2015).

- [11] Energy Education [https://energyeducation.ca/encyclopedia/Band\\$gap](https://energyeducation.ca/encyclopedia/Band$gap), 21.08.2022.
- [12] Weiss, C., Frais-Kölbl, H., Griesmayer, E., Kavrigin, P. Ionization signals from diamond detectors in fast-neutron fields. *The European Physical Journal A*, 52(9). doi:10.1140/epja/i2016-16269-8 (2016).
- [13] Kavrigin, P., Neutron and photon spectroscopy with diamond detectors https://indico.cern.ch/event/297045/sessions/146678/attachments/557272/767783/pavel_kavrigin_neutron_and_photon_spectroscopy_with_diamond_detectors.pdf 21.08.2022.
- [14] Schmidt B., Wetzig K., *Ion Beams in Materials Processing and Analysis*, Wien: Springer-Verlag, 2013.
- [15] Yao N. et al., *FOCUSED ION BEAM SYSTEMS Basics and Applications*, Cambridge: University Press, 2007.
- [16] Barschall H. H. et al., *Neutron Sources for Basic Physics and Applications*, Oxford: Pergamon Press, 1983.
- [17] Rolfs C. E., Rodney W. S., *Cauldrons in the Cosmos*, Chicago and London: The University of Chicago Press, 1983.
- [18] Anagnostopoulos K. N., *Computational physics*, Athens: National Technical University of Athens, 2016.
- [19] S. Agostinelli et al, *NIM A*, Vol. 506, pp. 250-303, 2003.
- [20] R. Brun and Rademakers, *NIM A*, Vol. 389, pp. 81-86, 1997.
- [21] McCluskey M. D., Haller E. E., *Dopands and Defects in Semiconductors*, Boca Raton: CRC Press, 2012.
- [22] Iliadis C., *Nuclear Physics of Stars*, Weinheim :WILEY-VCH Verlag GmbH & Co. KGaA, 2007.
- [23] Breese M. B. H., Jamieson D. N., King P. J. C., *Materials Analysis Using a Nuclear Microprobe*, New York:A Wiley-Interscience Publication JOHN WILEY & SONS, INC., 1996.

- [24] Lechner A., Particle Interactions with Matter, Proceedings of the CAS–CERN Accelerator School: Beam Injection, Extraction and Transfer, Erice, Italy, 10-19 March 2017, edited by B. Holzer, CERN Yellow Reports: School Proceedings, Vol. 5/2018, CERN-2018-008-SP (CERN, Geneva, 2018)
- [25] Thomson M., Modern Particle Physics, New York: Cambridge University Press, 2013.
- [26] G. Provas, M. Axiotis, I. Sandberg, V. Foteinou, S. Harissopulos, Hellenic Evolution of Radiation data processing and Modelling of the Environment in Space. IASA HERMES TN1.3. (2016).
- [27] Crnjac, A., Skukan, N., Provas, G., Rodriguez-Ramos, M., Pomorski, M., & Jakšić, M. (2020). Electronic Properties of a Synthetic Single-Crystal Diamond Exposed to High Temperature and High Radiation. *Materials*, 13(11), 2473. doi:10.3390/ma13112473
- [28] Cosic D., Provas G., Jaksic M., Begusic D. (2022.) Charge collection efficiency of scCVD diamond detectors at low temperatures. *Diamond and Related Materials* Volume 127, August 2022, (109184)
- [29] G. Santin et al., Nuclear Science, IEEE Trans., Vol. 52, pp. 2294-2299, 2005.